Ground states of quasi-two-dimensional correlated systems via energy expansion

Sam Mardazad,[1,*] Nicolas Laflorencie,[2,†] Johannes Motruk,[3,‡] and Adrian Kantian[1,§]
[1]*Institute of Photonics and Quantum Sciences, Heriot-Watt University, Edinburgh EH14 4AS, United Kingdom*
[2]*Laboratoire de Physique Théorique, CNRS and Université de Toulouse, 31062 Toulouse, France*
[3]*Department of Theoretical Physics, University of Geneva, Quai Ernest-Ansermet 24, 1211 Geneva, Switzerland*

(Received 31 March 2025; revised 21 October 2025; accepted 23 October 2025; published 25 November 2025)

We introduce a generic method for computing groundstates that is applicable to a wide range of spatially anisotropic 2D many-body quantum systems. By representing the 2D system using a low-energy 1D basis set, we obtain an effective 1D Hamiltonian that only has quasilocal interactions, at the price of a large local Hilbert space. We apply our new method to three specific 2D systems of weakly coupled chains: hardcore bosons, a spin-1/2 Heisenberg, and spinful fermions with repulsive interactions. In particular, we showcase a nontrivial application of the energy expansion framework, to the anisotropic triangular Heisenberg lattice, a highly challenging model related to 2D spin liquids. Treating lattices of unprecedented size, we provide evidence for the existence of a quasi-1D gapless spin liquid state in this system. We also demonstrate the energy expansion framework to perform well where external validation is possible. For the fermionic benchmark in particular, we showcase the energy expansion framework's ability to provide results of comparable quality at a small fraction of the resources required for previous computational efforts.

DOI: 10.1103/rgdt-msv6

I. INTRODUCTION

Quantum systems comprised of weakly coupled one-dimensional (1D) subsystems (c.f. Fig. 1) represent an important area in the study of correlated many-body physics. Not only are three different groups of repulsively-mediated superconductors in this class (the Bechgaard and Fabré salts [1,2], the "telephone-number" compounds [3,4], and chromium pnictide [5,6]), but so are Cs_2CuCl_4 [7–9] and Cs_2CuBr_4 [10,11], paradigmatic materials in the ongoing search for two-dimensional (2D) spin liquids [12–30]. As for their more isotropic siblings (e.g., cuprates for repulsively mediated superconductivity [31–33], κ-$(ET)_2Cu_2(CN)_3$ and $EtMe_3Sb[Pd(dmit)_2]_2$ for spin liquids [34–36]), progress on understanding the correlated phases of these materials at low temperatures has been famously slow, due to the outstanding difficulty of obtaining reliable theory for a great number of 2D correlated quantum systems.

At the same time, the spatial anisotropy of such materials has long been recognized as a significant potential advantage over their isotropic cousins, namely due to the uniquely powerful theoretical methods for the 1D subunits that make up these materials. The use of analytical Tomonaga-Luttinger liquid (TLL) theory [37] and matrix product state (MPS) numerics [38,39] has yielded insights for 1D correlated systems that are unmatched for higher-dimensional ones. Thus, for anisotropic 2D and three-dimensional (3D) models as well as for materials made up from weakly coupled 1D subunits, one strategy has been to leverage this unparalleled understanding of the 1D physics to the full, higher-dimensional system [40–43]. A striking early example of this is the 3D model materials for repulsively-mediated high-T_c superconductivity formed out of many doped two-leg Hubbard ladders [37,44]. Combining a TLL-description of the isolated ladders with a static mean-field (MF) treatment of the weak interladder tunneling yielded a conclusive description for the possibility of high-T_c superconductivity down to the level of repulsively mediated microscopic pairing, which remains an unrealized goal for isotropic 2D and 3D models to this day. More recently, this line of work has been further expanded on with the MPS + MF treatment of fermions, which allowed the first quantification of superconducting properties in these model materials, as well as resolving the competition with alternative insulating phases [45,46]. This MPS + MF framework for fermions had developed out of earlier MPS + MF approaches for anisotropic systems of either spins or bosons, for which the low-cost theoretical modeling of the magnetic BPCB compound had been a particularly noteworthy achievement [47–51]. This compound is one of numerous remarkable quasi-1D spin materials that exhibit nontrivial dimensional crossover effects, such as the $S = 1/2$ ladder $(C_7H_{10}N)_2CuBr_4$ (DIMPY) [52–55], or the $S = 1$ chain $NiCl_2$-$4SC(NH_2)_2$ (DTN) compound [56,57].

Yet the treatment of anisotropic correlated 2D systems by MF-decoupling the interactions between the 1D subunits

*Contact author: s.mardazad@hw.ac.uk
†Contact author: nicolas.laflorencie@cnrs.fr
‡Contact author: johannes.motruk@unige.ch
§Contact author: a.kantian@hw.ac.uk

Published by the American Physical Society under the terms of the Creative Commons Attribution 4.0 International license. Further distribution of this work must maintain attribution to the author(s) and the published article's title, journal citation, and DOI.

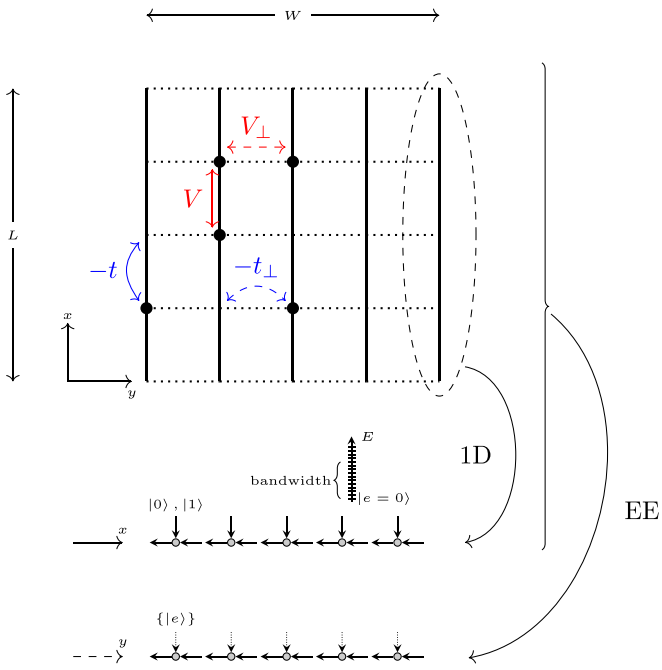


FIG. 1. Weakly interacting chains where particles can hop with transition probability $t = 1$ (—) or $t_\perp < t$ (- - - - -). All models we investigate also exhibit nearest neighbor repulsion with strength V along the chains, and some also contain such repulsion in the the perpendicular direction, of strength $V_\perp$.

has significant limitations. For all three existing classes of anisotropic repulsion-mediated superconducting materials, as well as for the spin liquid candidate materials Cs_2CuCl_4 and Cs_2CuBr_4, such decoupling is either inadmissable or ill-defined. One approach to exploit spatial anisotropy for these systems beyond static mean-field was chain dynamical mean field theory (chDMFT) [58,59]. It would treat a single 1D subunit—Hubbard chains with various repulsive short-range interactions—explicitly and would represent the rest of the system via a self-consistent hybridization function. But due to the underlying Quantum Monte Carlo (QMC) solver, this approach battles the exponential scaling to solution with decreasing temperature known as the sign problem, and would not be useful for any of the near-1D anisotropic superconducting materials. For spin systems such as those realized in Cs_2CuCl_4 and Cs_2CuBr_4, even setting up a chDMFT algorithm would be difficult due to the inherent geometric frustration.

Brute-force applications of MPS-based numerics such as the density matrix renormalization group (DMRG) to compute the ground states of 2D systems are generally also severely limited, especially when spatial anisotropy is large [22]. When these algorithms are confined to shared-memory parallelism, typically only long, narrow strips are feasible, as entanglement entropy grows rapidly with the width of the strip [60,61]. Distributed-memory parallelism as implemented in pDMRG can treat significantly wider systems, especially when combined with exploitation of the spatial anisotropy [62]. Nevertheless, even these high-performance implementations will rapidly struggle once the width of the strip approaches a significant fraction of its length. They also presuppose copious computational time and simultaneous access to many nodes of a high-performance supercomputer with fast internode connections.

In addition to multiple recent and prolific numerical developments [63–67], there are two other classes of algorithms geared at 2D correlated systems at low or zero temperature that are more generic, in that they do not presuppose a spatial anisotropy, and that aim to reduce resource requirements at the price of introducing approximations. These are projected entangled-pair states (PEPS), which represents a class of variational ansatz states built on higher-order tensor networks [68], and constrained-path or phase-free auxiliary-field Quantum Monte Carlo (AFQMC), which builds on the standard AFQMC for lattice fermions and purposefully removes the fermionic sign problem in different ways [69]. While these algorithms can be powerful, the level of their approximations can individually depend on the specific physical system. An approach such as PEPS, which is generally limited to low bond dimensions will also generally struggle to retain enough entanglement to describe an anisotropic system accurately in the strong-coupling direction.

What would be called for is a numerical technique that leverages the particular advantage inherent to spatially anisotropic problems, while also exhibiting only controlled approximation errors and being equally applicable to bosonic and fermionic systems.

In the present work, we introduce a generic numerical technique to calculate the many-body ground states of a variety of spatially anisotropic 2D quantum systems that are comprised of weakly coupled 1D subunits. The essence of this approach is to represent the system in the low-energy basis of the individual 1D subunits. This representation yields a new effective 1D Hamiltonian with a large local Hilbert space, spanned by those low-energy many-body states of the 1D subunits that are being retained, as sketched in Fig. 1. The error introduced by limiting the energy-width of the 1D basis set is a controlled one, in that the approach starts from the lowest lying excitations and systematically incorporates more and more higher-energy states; if all states could be retained, the full Hilbert-space of the 2D system would be recovered. As long as the energetic widths of the retained 1D-spectra exceed the coupling range of the interactions between the 1D subunits, this approach is able to capture the physics of the 2d ground state well and with surprisingly low computational effort. We demonstrate the algorithm's resulting ability to reach lattice sizes that would be infeasible with other controlled-approximation many-body numerics for both repulsively interacting fermions as well as frustrated spin systems. We point out that as the present work was concluded, we have become aware of a similar approach for arrays of coupled 1D continuum systems, but constrained to integrable models for which the 1D basis is known analytically [70,71].

The paper is organized as follows. In Sec. II we outline the main technical components of this approach, and discuss the use of symmetries to speed up calculations, how observables are computed, and the main sources of error. In Sec. III, we then show the concrete application of the energy expansion (EE) approach to obtain ground state properties for 2D Hamiltonians of spinless bosons, unfrustrated and frustrated spins, as well as repulsively interacting spinful fermions in a doped

regime. Where possible, here we also benchmark against alternative approaches in order to validate the EE-technique. Finally, in Sec. IV, we summarize the main strengths and drawbacks of the EE-technique, and discuss the outlook for its application to other concrete systems, as well as for further improving its performance and widening its scope.

II. METHOD

Without loss of generality, we can divide a 2D many-body system into chains running along the x axis, as shown, e.g., in Fig. 1. The Hamiltonian is split into terms which act only within the chains, labled by the y coordinate, which are subsumed into $\hat{H}_1$. The residual terms connecting different chains are collected in $\hat{H}_\perp$ respectively as also visualized in Fig. 1, i.e.,

$$\hat{H} = t\hat{H}_1 + t_\perp \hat{H}_\perp. \tag{1}$$

We assume that the magnitude of the matrix elements of $\hat{H}_1$ and $\hat{H}_\perp$ are of order 1. EE is applicable when the interchain coupling in Eq. (1) is small $t_\perp/t \ll 1$. Since $\hat{H}_1$ is purely 1D we can employ DMRG to efficiently compute its low-energy subspace [38]. We split it into the terms for the individual chains:

$$\hat{H}_1 = \sum_{y=1}^{W} (\hat{1}_1 \otimes \hat{1}_2 \otimes \ldots \otimes \hat{H}_y \otimes \ldots \otimes \hat{1}_W). \tag{2}$$

We generally suppress index y when focusing on a single chain. Our overall approach is to reexpress the total Hamiltonian Eq. (1), using the low-lying spectrum of the chains

$$\hat{H}|e\rangle = E_e|e\rangle. \tag{3}$$

Here, the index e is counting the excitations and $e = 0$ denotes the ground state. We obtain this spectrum sequentially, running a series of DMRG-based ground state searches, that incorporate orthogonality constraints for all previously found eigenstates (c.f. Appendix D 1). In general, the state $|e = 0\rangle$ has entanglement entropy scaling with surface area [60], however, most of the subunits we look at are gapless and thus have a log correction to the area law [72,73]. This makes the MPS ansatz efficient, but we also find the same to hold true for the low-lying eigenstates. In practice, we can go up to 60 to 100 energy eigenstates in the most relevant quantum number sectors, keeping less than 20 states in other sectors. On a further practical note, we remark that for the relatively short chains with periodic boundary conditions (PBCs) for which all 1D basis sets in the work have been obtained, a particularly efficient way to perform the calculations, is to implement the boundary condition with a single long-range coupling term from the first to the last site of the chain. Though this "naive" implementation of PBCs substantially boosts entanglement entropy and thus computational cost to obtain eigenstates, the increase of these costs for chains of modest length can be handled by any efficient, modern implementation of MPS-based eigensolvers. Crucially, the increase is more than offset by the very significant boost in stability and well-behaved convergence as one works ones way up the ladder of excited states, as the greatly increased entanglement entropy of the states turns out to be a key accelerant in avoiding false minima during the constrained eigenstate search.

Once the 1D subspace is obtained, we span a new 2D many-body basis using the tensor product

$$|\boldsymbol{e}\rangle = |e_1, \ldots, e_W\rangle, \tag{4}$$

where W denotes the number of chains, arrayed in y direction, as shown in Fig. 1. We now express Eq. (1) in terms of the 1D eigenstates by computing the matrix elements

$$\langle \boldsymbol{e}|\hat{H}|\boldsymbol{e}'\rangle = t\langle e_W \ldots e_1|\hat{H}_1|e'_1 \ldots e'_W\rangle + t_\perp \langle \boldsymbol{e}|\hat{H}_\perp|\boldsymbol{e}'\rangle \tag{5}$$

$$= t\sum_{y'} \left(\prod_{y=1}^{W} \delta_{e_y,e'_y} E_{e_{y'}} \right) + t_\perp \langle \boldsymbol{e}|\hat{H}_\perp|\boldsymbol{e}'\rangle, \tag{6}$$

using the eigenvector properties of the single-chain basis $|e\rangle$. The first term in Eq. (6) is a sum of identities on the subspace of the chosen energy eigenbasis of the chains. For each chain, which we will interchangeably denote a "supersite" in the following whenever represented by its low-energy basis, these identities are weighted with the energies of each basis state

$$\hat{E}_y = \hat{1}_1 \otimes \ldots \otimes \sum_{e_y} E_{e_y} |e_y\rangle\langle e_y| \otimes \ldots \otimes \hat{1}_W, \tag{7}$$

thereby effectively diagonalizing $\hat{H}_1$ in the 1D low-energy subspace. The nature of the second term in Eq. (6) depends on the specifics of the perpendicular part of the model and will thus be discussed in Sec. III for each of the models individually. Note that if all eigenstates of the chains are retained, the basis transformation would be exact.

Generally, this work focuses on interactions between chains that can be written as

$$\langle \boldsymbol{e}|\hat{H}_\perp|\boldsymbol{e}'\rangle = \sum_{xy} \langle e_W \ldots e_1|\hat{A}_{xy}\,\hat{B}_{x'y+1}|e'_1 \ldots e'_W\rangle \tag{8}$$

$$= \sum_{xy} \left(\delta_{e_1,e'_1} \ldots \langle e|\hat{A}_x|e'\rangle_y \langle e|\hat{B}_{x'}|e'\rangle_{y+1} \ldots \delta_{e_W,e'_W} \right), \tag{9}$$

where $\hat{A}_{xy}$ and $\hat{B}_{xy}$ denote operators acting locally around site x of chain y. For the purposes of the present work, we assume every chain to have the same Hamiltonian and all couplings between neighboring chains to be the same. We thus shift the y index from the operators and basis states onto the overlaps, as already done when going from Eqs. (8) to (9). However, the EE-framework does not depend on this assumption and it would be straightforwardly generalized to heterogeneous systems.

Heuristically, we find amplitudes $\langle e|\hat{A}_x|e'\rangle_y$ to be maximally of order $\mathrm{O}(10^{-1})$ for all studied systems. The actual values and magnitudes depend strongly on $|e\rangle$ and $|e'\rangle$, as exemplified in Fig. 2 for the creation operator in a HCB system. The main weight is accumulated in the bottom left corner, with clusters of transitions between the energetically higher excited states appearing as well.

Now that the full Hamiltonian Eq. (6) is expressed in terms of single-chain quantities that we can access, we can pick a method of choice for calculating the ground state of the resulting 2D Hamiltonian. We chose to employ DMRG again, which yields a Hamiltonian with nearest-neighbor coupling at

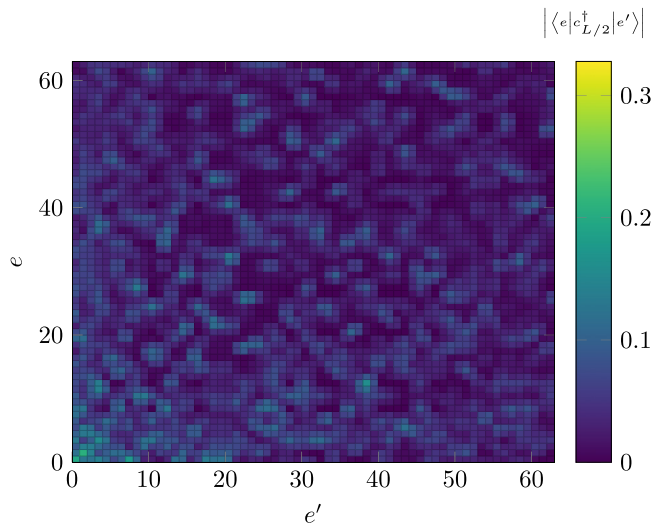


FIG. 2. Matrix elements of the creation operator in a HCB system of size $L = 16$ and nearest neighbor repulsion $V = 2$ going from $N = 8$ to $N = 9$ particles in the center of the chain.

most. Different to many other applications of the DMRG, the EE-framework has to wrestle with the large local Hilbert space $|e\rangle$ that we retain for each chain. We have found a sensible cutoff to be $d = 264$ for the bosonic or spin systems and $d = 384$ for the fermionic systems, which will be discussed further in Secs. II C and III. Thus, for the ability to perform actual calculations, the exploitation of conserved quantum numbers becomes even more essential than in most other applications of the DMRG.

A. Symmetries

All studied models exhibit $U(1)$ symmetries. The bosonic and spin models preserve particle number or z spin, respectively, while the fermionc model conserves both these quantum numbers simultaneously. This applies to Hamiltonian Eq. (1) as well as the individual chain Hamiltonians $\hat{h}_y$.

Therefore, we can make use of the usual decomposition of the tensor network entries into symmetry protected blocks when obtaining the 1D basis set [38,74–76]. This allows us to perform the orthogonalization procedure described in Eq. (D1) for states of the same sector only. It also eliminates many redundant entries in the EE Hamiltonian by restricting the number of elements to compute, as

$$\langle e|\hat{A}|e'\rangle = \langle e|\hat{A}|e'\rangle\delta_{\hat{\sigma}(e'),\hat{\sigma}(e)+T}, \tag{10}$$

with $\hat{A}$ an arbitrary single-chain operator and T its transformation behavior (i.e., the change in quantum number(s) effected by $\hat{A}$). Furthermore, $\hat{\sigma}$ denotes an operator mapping all quantum numbers of the respective energy eigenstate to their scalar eigenvalues σ, e.g.,

$$\hat{\sigma}(e) = (\{\sigma\}) = (n_e, z_e). \tag{11}$$

In this example, $\{\sigma\}$ denotes particle number n_e and the z-spin component z_e of the energy eigenstate e. For the overlaps of creation and annihilation operators it is $T = +1$ and $T = -1$, respectively, in the particle number sector, while for particle number operators $T = 0$. In practice, this means that any symmetry protected DMRG code can be repurposed for the EE framework after adjusting the irreducible representations for the local basis and reading in the new operator weights generated from the 1D basis set.

B. Measurements

In order to extract quantities beyond the energy and entanglement entropies from the EE-DMRG wave function, we need to establish a method to compute observables. However, working with the supersite tensor network, we have to be deliberate in defining our local operators to perform correct measurements. Matrix elements which act on one chain only, i.e., which have the same y component for all involved operators can be written as

$$\langle\psi|\hat{O}_{\boldsymbol{x},y}|\psi\rangle = \sum_{\sigma_y e_y e'_y} M^{\sigma_y e_y\dagger}\cdot M^{\sigma_y e'_y}\langle\sigma e|\hat{O}_{\boldsymbol{x}}|\sigma e'\rangle_y. \tag{12}$$

Note that the notation $\boldsymbol{x}$ implies the operator acting on any number of chain sites, i.e., $\hat{O}_{\boldsymbol{x},y}$ might be a particle number operator $\hat{n}_{x,y}$ or the entry of a correlator $c^\dagger_{x,y}c_{x',y}$ on any chain sites x and x'. However, we have to measure the full operator on the 1D system and cannot create it from more elementary operators, e.g.,

$$\begin{aligned}\langle\sigma e|\hat{n}_x|\sigma e'\rangle &= \langle\sigma e|\hat{c}^\dagger_x\hat{c}_x|\sigma e'\rangle \\ &\neq \sum_{e''=0}^{\tilde{d}-1}\langle\sigma e|\hat{c}^\dagger_x|\sigma'' e''\rangle\langle\sigma'' e''|\hat{c}_x|\sigma e'\rangle,\end{aligned} \tag{13}$$

since we usually truncate our system in 1D excitations $\tilde{d} < d$, as is described in Sec. II C. Furthermore, $M^{n_y e_y}$ is the tensor on supersite y for the e_y-th 1D state in sector(s) σ_y.

We made use of the fact that the MPS can be canonically normalized and therefore overlaps of local 1D supersites are identities for all but supersite y. In evaluating Eq. (12), we also exploit that our symmetry protected framework does not allow for changes in the global quantum numbers when computing observables. The quantity $M^{\sigma_y e_y\dagger}M^{\sigma_y e'_y}$ that appears in Eq. (12) is the reduced density matrix (RDM) of chain y. It contains all the information/probabilities for this chain extractable from the 2D wave function in the EE basis. The matrix elements are the individual weights of the 1D modes. Therefore, we only need to measure the transition elements $\langle\sigma e|\hat{O}_x|\sigma e'\rangle$ permitted by symmetry in 1D and can proceed with them as "local operators". Then measurements for supersite operators acting on single-chain Hilbert spaces can be executed in the ordinary way.

We also study observables acting on two chains, but the procedure can be generalized to more sites with some additional bookkeeping. Assuming an observable $\hat{O}_{\boldsymbol{x},yy'}$ acting on two chains y and y' and an arbitrary number of sites within the chains $\boldsymbol{x}$ we can write

$$\langle\psi|\hat{O}_{\boldsymbol{x},yy'}|\psi\rangle = \sum_{\substack{i_y i_{y'}\\ j_y j_{y'}}}\rho^{j_y j_{y'}}_{i_y i_{y'}}\langle i_y i_{y'}|\hat{O}_{\boldsymbol{x},yy'}|j_y j_{y'}\rangle \tag{14}$$

$$\begin{aligned}\rho^{j_y j_{y'}}_{i_y i_{y'}} = \sum_{i_{y+1}\ldots i_{y'-1}} &(M^{i_{y'}\dagger}M^{i_{y'-1}\dagger}\ldots M^{i_{y+1}\dagger}M^{i_y\dagger} \\ &\cdot M^{j_y}M^{i_{y+1}}\ldots M^{i_{y'-1}}M^{j_{y'}}),\end{aligned} \tag{15}$$

where have defined the two chain density matrix ρ and assumed $y < y'$ without losing generality. Note that we introduced the abbreviation $i_y = (\sigma e)_y$, as the quantum numbers of one of the two chains might now change along with an adjoint change $j_{y'} = (\sigma' e')_{y'}$ on the other chain. At the same time, the two-chain density-matrix ρ is never explicitly computed, as its size will scale as $\tilde{d}^4$. Generally, ρ it is a nonlocal quantity as one needs to contract all tensors in between the chains y, y'. However, many observables of interest factorize in the different chain-Hilbert spaces and therefore we can write

$$\langle i_y i_{y'}|\hat{O}_{\boldsymbol{x},yy'}|j_y j_{y'}\rangle = \langle i_y i_{y'}|\hat{O}_{\boldsymbol{x},y}\hat{O}_{\boldsymbol{x},y'}|j_y j_{y'}\rangle \tag{16}$$

$$= \langle \sigma e|\hat{O}_{\boldsymbol{x}}|\sigma' e'\rangle_y \langle \sigma e|\hat{O}_{\boldsymbol{x}}|\sigma' e'\rangle_{y'}. \tag{17}$$

This simplifies calculation tremendously since it means we can measure the operators for all basis states of the 1D set and proceed with them as local operators again. Two-chain measurements are thus reduced to regular expectation values, using the EE wave function and these supersite operators in the conventional manner: apply the local gate on site y' and contract the tensor train up to site y where another local gate is then applied.

C. Error sources

Practical application of the EE framework beyond very small systems entails some unavoidable yet controlled approximations. The derivation of the first term of Eq. (6) only requires the application of $\hat{H}_1$ to the basis state being proportional to the state itself and the 1D states to be orthonormal. The former can be controlled by computing the basis state's variance and the later by checking the overlaps with other states and imposing a threshold which we chose to be $\delta = 10^{-12}$

$$\langle e|\hat{H}_1^2|e\rangle - \langle e|\hat{H}_1|e\rangle^2 \leqslant \delta \quad \forall e = 0, \ldots, d-1, \tag{18}$$

$$\langle e|e'\rangle \leqslant \delta \quad \forall e, e' \text{ such that } \hat{\sigma}(e) = \hat{\sigma}(e'). \tag{19}$$

The second term in Eq. (6) can be computed exactly for many Hamiltonians by evaluating matrix elements of the 1D system, as described in Sec. II B. Yet, the number of single-chain basis states $|e\rangle$ that are retained will always have to be a small slice of the exponentially growing Hilbert space of the single-chain eigenbasis.

Crucially, only a limited number of this large set is necessary to describe the system accurately when interchain coupling $t_\perp$ is small. In the limit $t_\perp \to 0$ the system will minimize its energy by occupying the lowest energy mode on all chains, i.e., forming a product state. As interchain coupling grows from zero, the system can lower its energy by coupling 1D eigenstates different from $|0\rangle$ to each other, but the spread of energies across which this coupling can take place will still be restricted by $t_\perp$. We thus do not expect to observe arbitrarily high 1D excitations, as these are especially costly in energy when $t_\perp$ is small.

We find that analyzing the energy spread of 1D states that appear with sufficient weight on the diagonal of the single-chain density matrix [c.f. discussion after Eq. (12)] is a suitable method for estimating the range of single-chain eigenstates that need to be retained, as demonstrated in Fig. 12. Assuming continuity with increasing excitation number, we suppress a mode if its excitation probability drops below a certain value. Sectors in which all excitation probabilities are below the truncated weight of the EE-MPS are dropped by the singular value decomposition (SVD) automatically. Of course, the above is no exact criterion because a mode i_y may only be suppressed on all chains when the excitation probability $P(i_1 \ldots i_y \ldots i_W) = |\langle i_1 \ldots i_y \ldots i_W|\psi\rangle|^2$ of this mode is negligible for all other $i_{y'}$. For all studied systems we find the diagonal of the single-chain density matrix to have a strongly peaked distribution around the central sector, as can be seen in Fig. 12. Usually, the ground state of $\hat{H}_1$ takes up more than 95% of the weight for weak coupling and some of the adjacent sectors lowest-energy states make up most of the remaining weight. This is followed by a long tail of states which are marginally important but which are still retained to obtain the highest precision possible for observables.

Another way of probing whether sufficiently many single-chain eigenstates have been included is whether a given set has the capacity to describe the expected physics of the 2D system correctly. For example, depending on lattice structure and the type and range of interactions, a 2D tight-binding bosonic model at zero temperature can exhibit Bose-Einstein condensation. One signature behavior of this are single particle correlators decaying to a constant at long distances. In contrast to that, the ground states of the individual $\hat{H}_1$-Hamiltonians can at best exhibit algebraically decaying correlations. Therefore, we investigate the matrix elements of different excited 1D states, $\langle e'|\hat{b}_x^\dagger \hat{b}_y|e\rangle$ (c.f. Fig. 16) and observe when and how strong they decay with distance. We found that once we start to retain 10 to 20 eigenstates in the most relevant quantum number sectors we pick up many cross-state correlators which no longer show decay with distance $|x - y|$.

Finally, one practical criterion for deciding whether the local Hilbert space of the individual 1D subunits has been chosen judiciously consists of checking the stability of observables as the size of this space is varied. We discuss a concrete example of this towards the end of Sec. III B 1.

The second source of error stems from the truncated weight of the 2D DMRG wave function obtained for the Hilbert space spanned by the $|\mathbf{e}\rangle$-vectors. This error is not only well known and perfectly controllable via the bond dimension, but its impact on chain-local observables is known [77]. By virtue of the entanglement "hidden" in the supersite basis, the bond dimension required to achieve low truncated weights in the EE-framework remains much below those values that would be necessary to reach comparable discarded weights with conventional brute-force DMRG calculations for 2D models [62]. Furthermore, whenever the truncated weight of the EE-DMRG was above that of the required accuracy, we used the standard extrapolation in bond dimension for chain-local observables in order to improve precision for those quantities.

In the following section, we demonstrate the application of the EE framework to models of hardcore bosons, unfrustrated and frustrated spins, as well as to doped, repulsively interacting fermions. This includes comparisons to other controlled-approximation techniques where possible, including QMC and massively parallelized brute-force DMRG.

III. MODELS AND RESULTS

A. Hardcore boson on square lattice

The first model for which we benchmark the EE framework are hardcore bosons on a square lattice with rectangular geometry, $L \neq W$. These systems can be treated with great accuracy using QMC techniques, which makes them perfect for a first round of benchmarking. We study lattices of size $L \times W$ with nearest-neighbor repulsion V on the same chain but not between chains, which corresponds to $V_\perp = 0$ in Fig. 1. The Hamiltonian elements of Eq. (1) read

$$\hat{H}_1 = -\sum_{xy}(\hat{b}^\dagger_{x,y}\hat{b}_{x+1,y} + \hat{b}^\dagger_{x+1,y}\hat{b}_{x,y}) + V/t \sum_{xy}\hat{n}_{x,y}\hat{n}_{x+1,y} \tag{20}$$

$$\hat{H}_\perp = -\sum_{xy}(\hat{b}^\dagger_{x,y}\hat{b}_{x,y+1} + \hat{b}^\dagger_{x,y+1}\hat{b}_{x,y}). \tag{21}$$

Here we apply PBCs in the x direction of strong coupling, and open boundary conditions (OBCs) in the y direction of weak coupling $t_\perp$. We note that it would be possible to choose PBCs in both directions, at the cost of additional computational complexity. We highlight that the coupling constants have been factored in these Hamiltonians such that they are consistent with Eq. (1). Applying the EE procedure according to Eq. (6) and with the definition from Eq. (7) implies

$$\hat{H} = t\sum_y \hat{E}_y - t_\perp \sum_{xy}(\hat{\beta}_y(x)^\dagger \hat{\beta}_{y+1}(x) + \hat{\beta}_{y+1}(x)^\dagger \hat{\beta}_y(x)), \tag{22}$$

where nondiagonal operators have been defined according to Eq. (17)

$$\hat{\beta}_y(x)^\dagger = \hat{1}_1 \otimes \ldots \hat{1}_{y-1} \otimes \sum_{nee'} \langle n+1, e|\hat{b}^\dagger_x|n, e'\rangle_y \times |n+1, e\rangle\langle n, e'|_y \otimes \hat{1}_{y+1} \otimes \ldots \otimes \hat{1}_W \tag{23}$$

$$\hat{\beta}_y(x) = \hat{1}_1 \otimes \ldots \hat{1}_{y-1} \otimes \sum_{nee'} \langle n, e|\hat{b}_x|n+1, e'\rangle_y |n, e\rangle \times \langle n+1, e'|_y \otimes \hat{1}_{y+1} \otimes \ldots \otimes \hat{1}_W. \tag{24}$$

Here, n is the particle number supplied by the application of the symmetry operator $\hat{\sigma}(e) = n$. The first term in Eq. (22) acts analogous to a chemical potential for the occupation of the 1D modes, while the second term reexpresses interchain hopping using the 1D basis states. We point out that the flow of quantum numbers due to application of a local operator is independent of the position within the chain x, which only affects the numerical values of the matrix elements. This helps to simplify the implementation of the framework.

The number of particles is chosen to be half the number of total orbitals, i.e., $N = LW/2$. This yields our choice for the 1D modes included in the local basis

$$\begin{aligned} \underline{|n_y - L/2| = 4}: &\quad 0 \leqslant e \leqslant 5, \\ \underline{|n_y - L/2| = 3}: &\quad 0 \leqslant e \leqslant 9, \\ \underline{|n_y - L/2| = 2}: &\quad 0 \leqslant e \leqslant 19, \\ \underline{|n_y - L/2| = 1 \text{ or } 0}: &\quad 0 \leqslant e \leqslant 63 \end{aligned} \tag{25}$$

by means of the heuristics outlined in Sec. II C, as well as checking for the convergence of observables such as the ground state energy and correlation functions with the size of the basis $|e\rangle$. For the system sizes studied here we thus settle on total local dimension of $d = 264$. This results in significant memory requirements, reaching up to 2 TB of RAM for a two-site DMRG update at a bond dimension of $m = 256$ and a real-valued wave function. The technical details to this are discussed in Appendix D.

The first validation of the EE-framework against zero-temperature QMC calculations (which provide data that are numerically exact within statistical errors fully controlled by the number of Monte Carlo steps [63]), is done for the ground state energy. The results are shown in Fig. 3. We observe correct physical behavior as V and $t_\perp$ are changed, the former increasing the energy per site as it grows, while the latter lowers it. Even more importantly, we obtain good agreement with the QMC gold standard for this type of model as shown in Fig. 3. With the truncated weight of the final wave function being $O(10^{-12}..10^{-8})$, we could dispense with the extrapolation to infinite bond dimension in this case. The same holds true for the measurement of a simple density-density correlation

$$\langle\psi|\hat{n}_{x,W/2}\,\hat{n}_{L/2,W/2}|\psi\rangle \tag{26}$$

which again yields relative errors of the order of permills compared to exact QMC, as is displayed in Fig. 3(c).

B. Spins on square and triangular lattice

Here, we study the performance of the EE framework for 2D spin-1/2 systems. First, we test the ability of this new approach to capture ordered many-body quantum states for a case that is still amenable to exact validation via QMC, the anisotropic Heisenberg quantum antiferromagnet (AFM) in the absence of frustration. Building on that, we then showcase the power of the EE framework for a notoriously difficult problem in the domain of strongly correlated 2D systems, the conjectured spin liquid states on the anisotropic triangular lattice. With the ability to address significantly larger 2D lattices than other many-body numerics, we demonstrate the ability to sort through the predictions of several competing theories for the conjectured ground states of this model. In both cases, we study a spin-1/2 Heisenberg Hamiltonian

$$\hat{H} = J\sum_{\langle i,j\rangle_x} \hat{\mathbf{S}}_i\hat{\mathbf{S}}_j + J_\perp \sum_{\langle i,j\rangle_\perp} \hat{\mathbf{S}}_i\hat{\mathbf{S}}_j, \tag{27}$$

with antiferromagnetic coupling $J, J_\perp > 0$. The notation $\langle i, j\rangle_x$ implies nearest neighbors in x direction only, while $\langle i, j\rangle_\perp$ denotes nearest neighbors in the perpendicular direction, a set of bonds that will be different between the square and the triangular lattice (c.f. Figs. 1 and 4). The operators are defined in the standard way, $\hat{\mathbf{S}}_i = (\hat{S}^x_i, \hat{S}^y_i, \hat{S}^z_i)^\intercal$ being a vector of spin-1/2-operators on site $i = (x, y)$. In this subsection, we also always consider a square-shaped geometry, i.e., $L = W$.

1. Square lattice: anisotropic Heisenberg antiferromagnet

We exploit that the Heisenberg Hamiltonian in the $S_z = 0$ subspace can be mapped to hardcore bosons at half filling, as recapped in Appendix G. While the spin-spin-coupling in

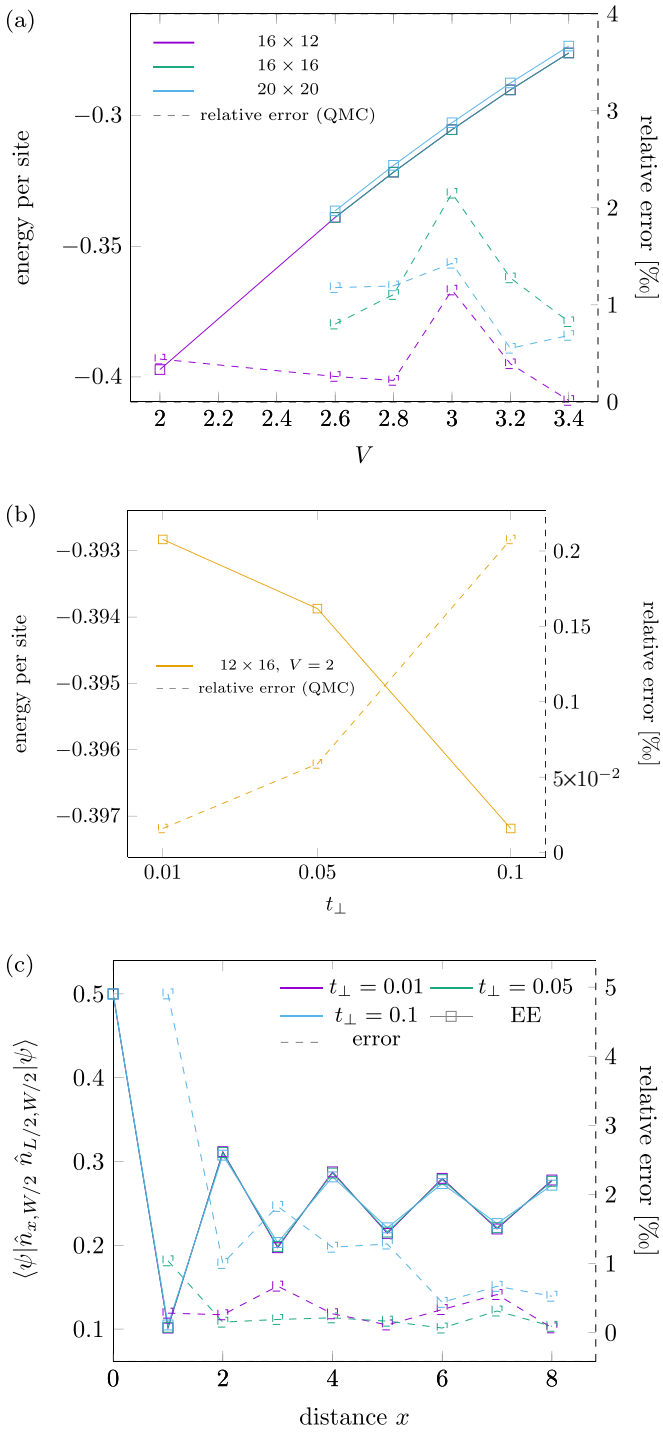


FIG. 3. Panels (a), (b) show the energies of the system scaling with intrachain density repulsion and interchain coupling, respectively. In the former case, $t_\perp$ was fixed to be 0.1 while in the latter $V = 2$. Panel (c) shows the correlator Eq. (26) along the strong coupling direction for different intrachain couplings $t_\perp$ of a 16×12 strip with repulsion $V = 2$. The relative error compared to exact QMC data is shown on the right-hand y axis (- - -).

the z direction leads to an additional density-density interaction term in the direction of transverse coupling compared to Sec. III A, we can keep using the local basis Eq. (25). We therefore require comparable resources, except for the growth

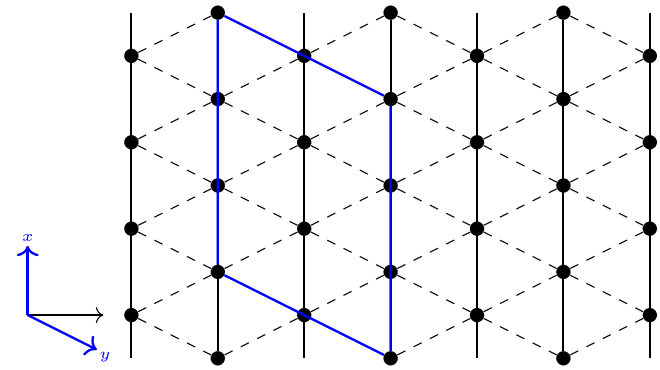


FIG. 4. Triangular lattice made up of weakly coupled chains where spins interact with coupling strength $J = 1$ (—) or $J_\perp$ (- - -). The blue lines (—) show the choice of our elementary vectors. The unfinished lines in x direction indicate PBCs while the horizontal direction has OBCs.

of the EE-for the growth of the EE-matrix product operator (MPO) bond dimension.

Analogous to the mapping that yields Eq. (22) from Eqs. (20) and (21), for the square lattice we thus obtain

$$\hat{H}_\square = J \sum_y \hat{E}_y + J_\perp \sum_{xy} (\hat{\beta}_y(x)^\dagger \hat{\beta}_{y+1}(x) + \text{H.c.}) + 2J_\perp \sum_{xy} \hat{\eta}_y(x)\hat{\eta}_{y+1}(x) \tag{28}$$

from the original Hamiltonian, Eq. (27). The definition of the supersite operators $\hat{\beta}$ and $\hat{\beta}^\dagger$ is the same as in Eqs. (23) and (24), exploiting the standard mapping of spin-1/2 operators to HCB, i.e., $\hat{b}^\dagger := \hat{S}^x + i\hat{S}^y$ (c.f. Appendix G). Complementing these operators is the local density operator expressed in the 1D basis of the chains

$$\hat{\eta}_y(x) = \hat{1}_1 \otimes \ldots \sum_{nee'} \langle n, e|\hat{n}_x|n, e'\rangle_y |n, e\rangle\langle n, e'|_y \ldots \otimes \hat{1}_W . \tag{29}$$

This operator appears again during the mapping of spins to HCB, $\hat{n} := \hat{S}^z + 1/2$.

Our primary aim in studying the ground state of $\hat{H}_\square$ is to quantify the capacity of the EE framework to describe ordered states of 2D many-body systems. To achieve this goal, we exploit that the underlying Hamiltonian Eq. (27) on a square lattice can be treated with high efficiency using QMC techniques, such as the stochastic series expansion (SSE) [78]. This technique scales linearly in the number of lattice sites and inverse temperature, with the statistical error decreasing with the square root of the independent Monte Carlo samples. For the range of parameters that we target here, SSE-QMC renders a benchmark that is exact for all practical purposes.

To gauge the performance of the EE-technique against the QMC gold standard, we focus on the spin-spin correlation functions both along one of the two central chains as well as along the perpendicular coupling direction

$$C(x) = \langle\psi|\hat{S}^z_{c,c}\hat{S}^z_{c+x,c}|\psi\rangle, \tag{30}$$

$$C_\perp(y) = \langle\psi|\hat{S}^z_{c,c}\hat{S}^z_{c,c+y}|\psi\rangle, \tag{31}$$

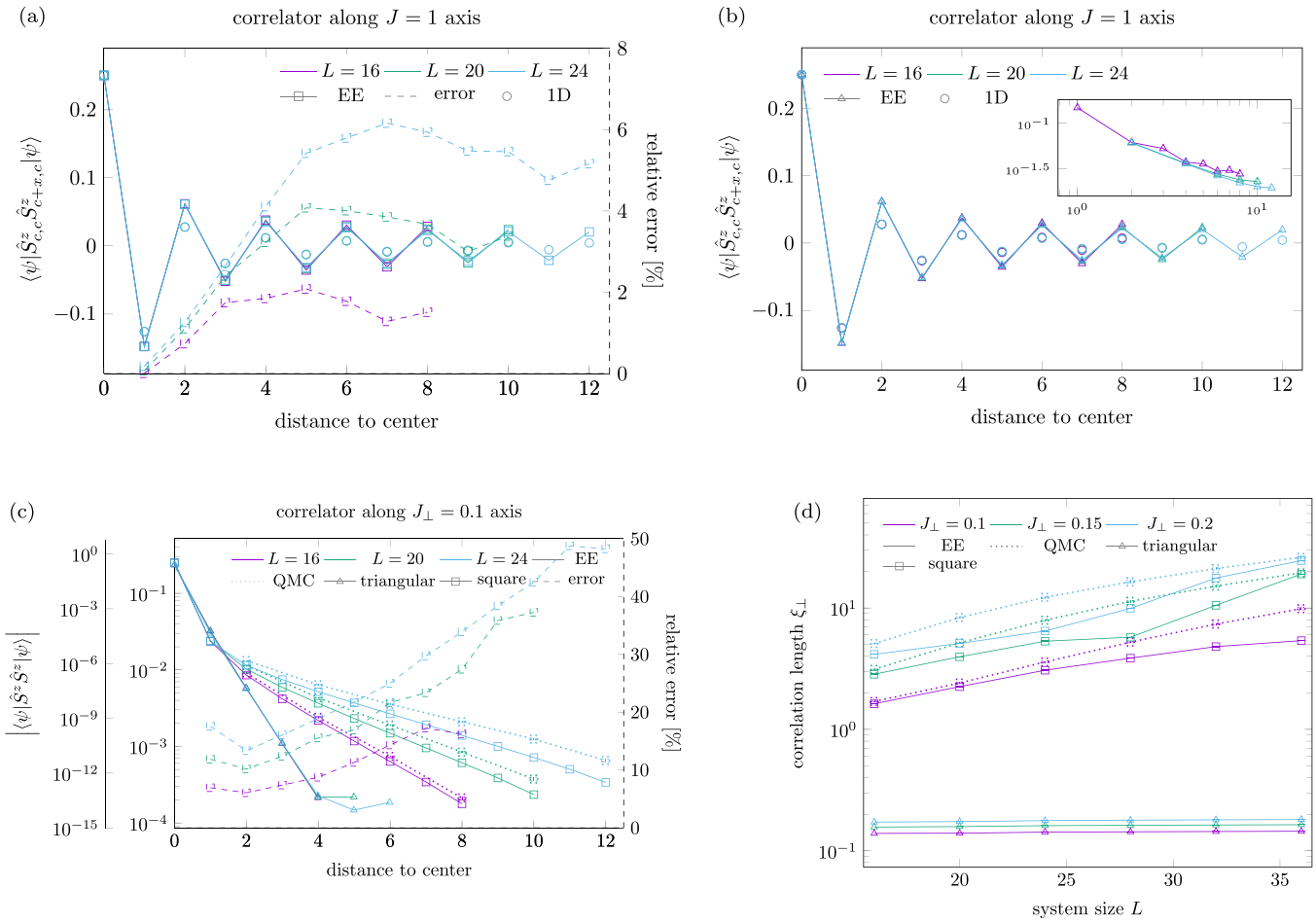


FIG. 5. Panels (a), (b) show the algebraic decay of the S^zS^z-correlator for $L = 16, 20, 24$ along the strong coupling direction and with an interchain coupling of $J_\perp/J = 0.1$ for the square (□) and the triangular (△) system, respectively [c.f. discussion below Eqs. (31) and (34)]. The inset of Panel (b) shows $|C(x)|$ on a double logarithmic scale. Panel (c) shows $|C_\perp(y)|$ at $J_\perp = 0.1$ (c.f. discussion in main text). Panel (d) shows the perpendicular correlation length $\xi_\perp(L)$ for multiple values of $J_\perp = 0.1, 0.15, 0.2$.

where $c = L/2 = W/2$ picks out one of the four central sites in our chosen lattices, for which both L and W are even. As shown in Fig. 5(a), the EE framework matches the QMC benchmark very well in the strong-coupling x direction, the error in the correlator even at maximal distance reaching at most 6% for the largest lattice ($L = W = 24$). In the transverse direction, where correlations are naturally significantly weaker, the EE-based calculations see a stronger increase in error as the system size grows, even at the lowest $J_\perp$-value, as illustrated in Fig. 5(c).

Nevertheless, the EE approach still captures the existence of an ordered anisotropic AFM state [40,42,55]. Indeed, in the regime $J_\perp \ll J$ for finite lattices, the transverse correlations are found to decay with a W-dependent exponentially decaying envelope,

$$|C_\perp(y)| \propto \mathrm{e}^{-y/\xi_\perp(W)}, \tag{32}$$

but the length-scale $\xi_\perp(W)$ associated with this decay itself grows at least linearly with the value of W, recovering the ordered AFM in the thermodynamic regime. As summarized in Fig. 5(d), both our EE framework and the QMC benchmarks correctly capture this physical behavior for a range of small $J_\perp/J$-values.

While the EE approach is capable of reproducing the correct physics, it does underestimate the magnitude of $\xi_\perp(W)$ systematically compared to the QMC benchmark. This systematic error grows with lattice size and the value of $J_\perp/J$. This trend is to be expected, for two reasons: (1) As L grows, the size of the retained single-chain basis $|e\rangle$ would need to increase exponentially if every state within the retained bandwidth of energy contributed equally. In practice we observe that at the level of the weights on the diagonal of the single-chain RDM, more than 90% of the weight is in the ground state of $\hat{H}_1$, with some additional percentages for the first excited state of the quantum number sector of that ground state, as well as to the ground states of the adjacent sectors. Beyond that, in every relevant quantum number sector, the higher in energy a state $|e\rangle$ is relative to that sector's ground state $|0\rangle$, the less it contributes to the 2D wave function in general. At the same time, there is also a significant variation, with a long tail of states with spiking contributions that will be increasingly difficult to incorporate as L is increased, as illustrated in Fig. 12. Still, we find that observables appear to converge in the size of the retained basis set $|e\rangle$ of the chains, for which examples are shown in Fig. 17. (2) Even though the targeted state is ordered, the entanglement entropy of the 2D

wave function scales with subsystem boundary. Consequently, the truncated weight increases strongly when the maximal bond dimension is fixed to the RAM-limited value of 256, as shown in Fig. 11. Toward the upper range of L and $J_\perp$, we observe that the truncated weight begins to saturate, clearly due to an insufficient bond dimension.

There are ways to mitigate the RAM bottleneck and increase the bond dimension, as discussed in Appendix D 3. As the present study of the AFM ordered state on the anisotropic Heisenberg model on the square lattice is a proof of principle, we do not pursue these alternatives further here.

2. Triangular lattice: quasi-1D spin liquid

The Heisenberg model, Eq. (27), placed on the anisotropic triangular lattice (c.f. Fig. 4) has been subject to a number of previous studies. These are motivated by the realization of this model—or a close variant of it—in Cs_2CuCl_4 and Cs_2CuBr_4, which are believed to host quantum spin liquid states [9]. Previous theoretical work yielded conflicting predictions for the ground or low-temperature state of this model in the physically relevant regime of $J_\perp \ll J$ [12–25,27,29,30]. This is due to the substantial technical difficulty in obtaining solutions for larger lattices. Not only are any QMC-based techniques incapable of addressing even moderately sized lattices at low or zero temperature due to the sign-problem, which is caused by the frustrated nature of nearest-neighbor coupling in this type of lattice. Also, attempts at brute-force application of the DMRG-algorithm to these 2D systems are made difficult exactly by the anisotropic nature of the lattice: a low ratio of $J_\perp/J$ causes a failure to converge in any standard zigzag mapping in the y direction [22]. The alternative, which would be to combine a mapping in the x direction with pDMRG, would require simultanous access to many compute notes over a sustained period, and even then it is possible that this approach would not be able to treat many chains [62].

The EE-approach however is tailor-made for this regime, as the frustrated nearest-neighbor coupling can be expected to reduce entanglement between chains, and thus the bond dimension required to efficiently approximate the true 2D ground state with the underlying choice of MPS-representation (c.f. Fig. 1). Using the lattice and coordinate definitions shown in Fig. 4, we obtain the EE-Hamiltonian $\hat{H}_\triangle$ for this lattice by adding to Eq. (28)

$$\hat{H}_\triangle = \hat{H}_\square + J_\perp \sum_{xy} (\hat{\beta}_y(x)^\dagger \hat{\beta}_{y+1}(x+1) + \text{H.c.}) + 2J_\perp \sum_{xy} \hat{\eta}_y(x)\hat{\eta}_{y+1}(x+1). \tag{33}$$

Along with this, we also use a modified definition of the transverse correlator,

$$C_\perp(y) = \langle\psi|\hat{S}^z_{c,c}\hat{S}^z_{c+y,c+2y}|\psi\rangle, \tag{34}$$

which takes the triangular structure of the lattice into account, where equivalent sets of sites in the direction perpendicular to the x axis will be found only on every second chain.

Our results conclusively show the suitability of the EE framework for these anisotropic frustrated systems. While correlations $C(x)$ in the strong-coupling direction are actually slightly enhanced over the isolated case as shown in Fig. 5(b), the correlator $C_\perp(y)$ is massively depressed when compared to the anisotropic square lattice, as shown in Fig. 5(c). More importantly, the exponential decay of these correlations with distance appears to exhibit almost no dependence on the size of the system. Therefore, the correlation length $\xi_\perp$, that can be extracted from fitting, almost does not change with L and W as summarized in Fig. 5(d), and increases only sublinearly with $J_\perp/J$, c.f. Fig. 6. This is accompanied by a drastic decrease in the truncated weight as shown in Fig. 11, while maintaining the same value of the bond dimension, $m = 256$, as for the square lattice. Complementing this is the observation that even more of the weight of the single-chain RDM is shifted to the ground state of the isolated chain than in the case of the square lattice, as shown in Fig. 12.

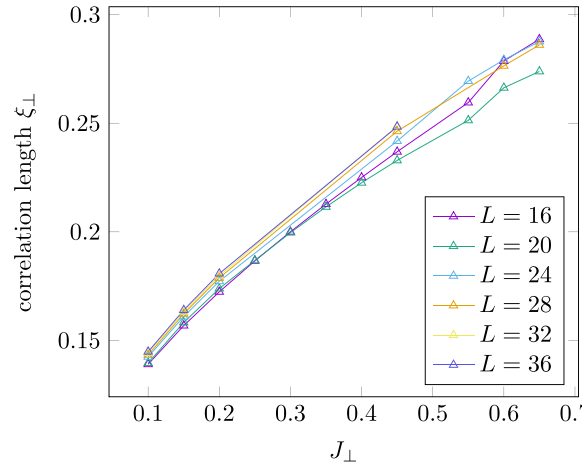


FIG. 6. Length-scale $\xi_\perp$ for transverse correlations as a function of $J_\perp$ for triangular lattices of different sizes.

The ability of the EE-technique to treat this lattice at unprecedented sizes with controlled-approximation many-body numerics allows to draw inferences about the possible nature of the ground state of this model, which is the subject of intense and conflicting research. The strong suppression and size-independence of $C_\perp(y)$, coupled with the apparently algebraic behavior of $C(x)$ appears to support those works that predict this model to realize a gapless quasi-1D spin liquid at low $J_\perp/J$ [13,30]. Thus, our results seem incompatible with work that indicated an AFM at low $J_\perp/J$ due to higher-order processes [16]. At the same time we cannot rule out with absolute certainty that the AFM order predicted in [16] isn't so weak that it cannot be resolved even by the unprecedented lattice sizes accessible to our framework. Likewise, we find no sign that this model exhibits a phase transition around $J_\perp/J \approx 0.6$. Such predictions had been based on ground state energies obtained from variational Quantum Monte Carlo (vQMC) calculations [25], as well as series expansion [29]. However, our EE-calculated energies substantially improve upon those obtained from vQMC, as shown in Fig. 7. Not only do we observe no change in the slope of the energy per site with changing $J_\perp/J$ around 0.6 (c.f. Fig. 7), but the entanglement entropy, another possible indicator of a quantum phase transition, also does not exhibit distinguishing features for any $J_\perp/J \leqslant 0.65$.

The low truncated weights that we find at small $J_\perp/J$ for the triangular lattice and the large bandwidth of energies

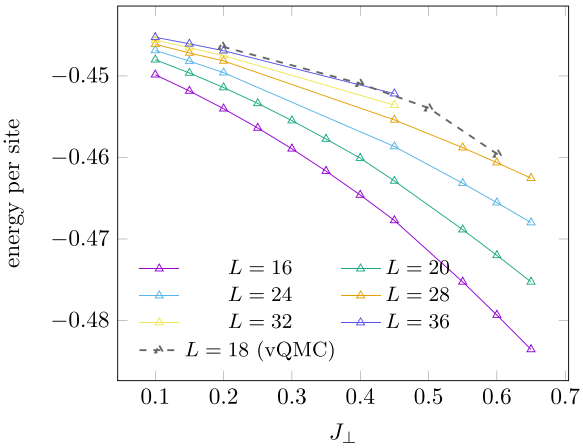


FIG. 7. Energies for different system sizes and intrachain couplings $J_\perp$ of the triangular lattice compared to vQMC data extracted from [25] for a 18×18 sites system.

spanned by the single-chain basis states that we incorporate (c.f. Figs. 11 and 12, respectively) makes it likely that the EE-framework approximates the ground state wave function well in these cases. But despite the large lattices amenable to the EE-framework, we are prevented from drawing definite conclusions about the actual ground state properties of the model at this point, and will return to this question in future work. That is because we have encountered persistent problems in converging the wave function once a finite flux through the periodic direction is inserted into the Hamiltonian in order to locate states with spiral ordering that could compete with the quasi-1D spin liquid [22]. This flux insertion needs to be performed in two places, namely both in the single-chain Hamiltonian, and in the effective EE-Hamiltonian. The former is done by taking the first term of Eq. (27), where the nearest-neighbor spin-flipping terms are modified, i.e.,

$$\hat{S}^+_{x,y}\hat{S}^-_{x+1,y} + \hat{S}^+_{x+1,y}\hat{S}^-_{x,y} \to \mathrm{e}^{\mathrm{i}\phi}\hat{S}^+_{x,y}\hat{S}^-_{x+1,y} + \mathrm{e}^{-\mathrm{i}\phi}\hat{S}^+_{x+1,y}\hat{S}^-_{x,y}. \tag{35}$$

From the resulting isolated-chain Hamiltonian $\hat{H}_1(\phi)$ a new basis set $|e(\phi)\rangle$ needs to be constructed for every ϕ-value of interest. A matching flux also needs to be inserted into $\hat{H}_\perp$ in the EE-representation, which we do by modifying the diagonal tunneling terms in Eq. (33):

$$\begin{aligned}&\hat{\beta}_y(x)^\dagger\hat{\beta}_{y+1}(x+1) + \hat{\beta}_{y+1}(x+1)^\dagger\hat{\beta}_y(x)\\ &\quad\to \mathrm{e}^{\mathrm{i}\phi}\hat{\beta}_y(x)^\dagger\hat{\beta}_{y+1}(x+1) + \mathrm{e}^{-\mathrm{i}\phi}\hat{\beta}_{y+1}(x+1)^\dagger\hat{\beta}_y(x).\end{aligned} \tag{36}$$

In principle, searching for the flux value that minimizes the energy of the 2D ground state would allow to test how the model transitions to a state with generically incommensurate spiral order as $J_\perp/J$ grows. Such spiral order has to appear at some point, either continuously or due to a quantum phase transition [13,15,18,22,29,30,79]. However, in practice we have found it difficult to obtain converged wave functions at $\phi \neq 0$. We have not yet identified the cause of this challenge, which grows pronouncedly with increasing $J_\perp/J$. Mitigating action, such as switching to single-site DMRG-updates is discussed in more detail in Appendix D 3. This would be done with the aim of being able to increase bond dimension significantly within the constraints of RAM, in order to pull free of the manifold of metastable states that appears at finite flux. However, in this instance we have found no benefit from this approach so far, with energies only decreasing marginally on what in the overwhelming number of cases are still clearly metastable excited states of the effective 2D Hamiltonian.

C. Fermions on square lattice

Our final systems are spin-1/2 fermions on a square lattice with rectangular geometry, $L \neq W$. In general, stiff systems of weakly coupled 2D Fermi-Hubbard chains with repulsive interactions are minimal models for superconductivity as well as competing insulating phases in the organic Bechgaard and Fabré salts, and have been studied as such [62,80]. Generally, this is outstandingly difficult for controlled-approximation many-body calculations, for the same reasons as for the isotropic 2D-Hubbard model of the high-T_c superconductors: the sign-problem for QMC techniques, superlinear growth of entanglement-entropy with subsystem surface area for MPS-based algorithms [81]. Here, we want to provide a proof-of-concept study for the capacity of the EE-framework to obtain results of comparable quality to those obtained from massively parallelized pDMRG at a small fraction of the computational effort, which moreover can treat far wider lattices, and thereby actually address the 2D limit. The $U-V$-model of the Bechgaard and Fabré salts has the following form:

$$\begin{aligned}\hat{H}_1 = &-\sum_{xy,\tau=\uparrow\downarrow}(\hat{c}^\dagger_{\tau,xy}\hat{c}_{\tau,x+1y} + \hat{c}^\dagger_{\tau,x+1y}\hat{c}_{\tau,xy})\\ &+ U/t\sum_{xy}\hat{n}_{\uparrow\downarrow,xy} + V/t\sum_{xy}\hat{n}_{xy}\hat{n}_{x+1y},\end{aligned} \tag{37}$$

$$\hat{H}_\perp = -\sum_{xy}(\hat{c}^\dagger_{\tau,xy}\hat{c}_{\tau,xy+1} + \hat{c}^\dagger_{\tau,xy+1}\hat{c}_{\tau,xy}), \tag{38}$$

where $c^{(\dagger)}_{xy}$ are now the fermionic creation and annihilation operators on the respective site and chain, $\hat{n}_{\uparrow\downarrow,x,y}$ counts the number of doublons, and generally $U \gg V > t \gg t_\perp$.

In principle, we can apply the same EE as in Eq. (6) to Eqs. (37) and (38) and obtain a new supersite Hamiltonian. However, additional care must be taken due to the fermionic nature of the basis spanning the Hilbert space, i.e., we transform Eq. (38) to be

$$\langle \boldsymbol{i}|\hat{H}_\perp|\boldsymbol{i}'\rangle = -\sum_{xy,\tau}[\langle i_W \dots i_1|\hat{c}^\dagger_{\tau,xy}\hat{c}_{\tau,xy+1}|i'_1 \dots i'_W\rangle + \text{H.c.}] \tag{39}$$

$$= -\sum_{xy,\tau}\left[\prod_{j=1}^{y-1}\left((-1)^{n_j}(-1)^{n'_j}\delta_{n_j n'_j}\right)(-1)^{n'_y}\langle i|\hat{c}^\dagger_{\tau,x}|i'\rangle_y\langle i|\hat{c}_{\tau,x}|i'\rangle_{y+1}\prod_{j=y+2}^{W}\delta_{n_j n'_j} + \text{H.c.}\right]. \tag{40}$$

Here, $i = (n, z, e)$ again counts the 1D eigenstate basis divided into its subsector through particle number and spin. Furthermore, we recognize the regular Jordan-Wigner transformation of "local" operators where the active site is mediating between the local orbitals and introduces signs. However, now the mediation happens by means of matrix elements of the 1D basis. Apart from that, sites to the right of the active site are identities and sites to the left of it are parity operators counting the total occupation per chain. Squaring the parity gives the identity which effectively makes all the sites left of y trivial. Nevertheless, writing it in this way helps when implementing supersite local operators in code. Thus, creation and annihilation operators read

$$\hat{\gamma}_y(\tau, x)^{(\dagger)} = \hat{P}_1 \otimes \ldots \otimes \hat{P}_{y-1} \otimes \sum_{ii'} \langle i|\hat{c}^{(\dagger)}_{\tau,x}|i'\rangle |i\rangle\langle i'| \otimes \hat{1}_{y+1} \otimes \ldots \otimes \hat{1}_W \tag{41}$$

with the parity operator $\hat{P}_y = (-1)^{\hat{n}_y}$, which is generalized to the total number-operator $\hat{n}_y = \sum_x \hat{n}_{x,y}$ for chain y instead of the number of particles on a site. Note that by exploiting symmetries it yields that the only nonzero matrix elements are

$$\langle n+1, z+\tau, e|\hat{c}^\dagger_{\tau,x}|n, z, e'\rangle \tag{42}$$

$$= \langle n, z, e'|\hat{c}_{\tau,x}|n+1, z+\tau, e\rangle^*. \tag{43}$$

With this definition, the perpendicular Hamiltonian reduces drastically to

$$\hat{H}_\perp = -\sum_{xy,\tau} [\hat{\gamma}_y(\tau, x)^\dagger \hat{\gamma}_{y+1}(\tau, x) + \hat{\gamma}_{y+1}(\tau, x)^\dagger \hat{\gamma}_y(\tau, x)], \tag{44}$$

which we recognize as the hopping between supersites.

We now want to investigate $L \times W$ strips again, this time with OBCs in both directions to ease comparison with prior work that was done in the same manner. Due to the known density of itinerant charge in the quasi-1D Bechgaard and Fabré salts we focus on $N = LW/2$ [2], which means we can use the particle number sectors $0 \leqslant n \leqslant L$ for the 1D basis set again. However, technically sectors $n > L$ are also possible, they are just heavily suppressed due to the strong repulsive interactions. This also means we can restrict ourselves to supersite occupation numbers $0 \leqslant n_y \leqslant L$, even though, we restrict this number in practice even further, as is discussed in Appendix C. Running a quick EE-DMRG with low bond dimension and evaluating the chain RDM in the center of the system yields the symmetry sectors and respective number of excitations in Table I. The interchain coupling is chosen to be $t_\perp/t = 0.1$, a typical value for the Bechgaard and Fabré salts [2]. For the electron interactions, we used $U/t = 4$, $V/t = 1$. While these values are not quite representative for those obtained from actual materials, they allow us to compare to preexisting data.

For the benchmark, we again compare both energies per site and correlation functions to previous results obtained from brute-force distributed-memory DMRG calculations at high bond dimension. The comparison of the energy densities is shown in Fig. 8. The chains coupled with a bond dimension of $m = 512$ are around a permill higher in energy than those

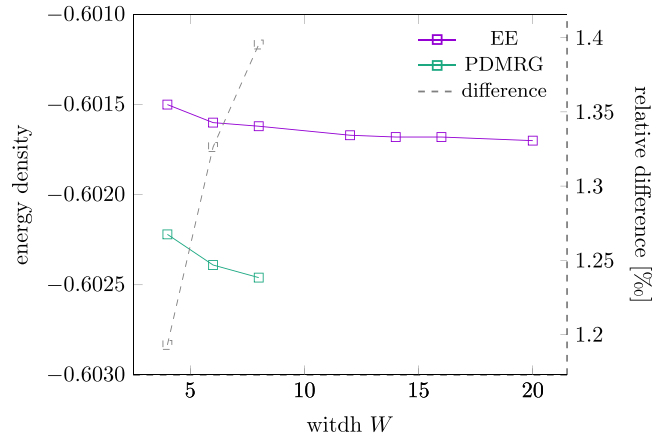


FIG. 8. EE groundstate energy of an $20 \times W$ strip of fermions with on-site and nearest neighbor repulsion $U = 4$ and $V = 1$, respectively. Both directions have OBCs and the system is at quarter filling $N = LW/2$. The chains are coupled with $t_\perp = 0.1$. The EE results are obtained with bond dimension $m = 512$ while the multinode DMRG from [62] used a bond dimension of $m = 18$ k. The relative difference on the right y axis (- - -) is of the order of a permill.

of the brute-force calculations performed with $m = 18$ k. Whether this difference originates from the lower interchain entanglement or the truncated local Hilbert space will be the subject of future work. In any case, further mitigation would demand more RAM to be accessible.

Since the hopping in perpendicular direction is weak, the mapping of the 2D system to MPS in [62] had to be done in the strong-coupling direction in order to achieve convergence. In practice, this leads to a hopping range of length L for the perpendicular tunneling for each site, necessitating the high bond dimension to converge the system. This makes it very demanding to scale the system in the perpendicular direction using the brute-force approach. In contrast, EE can readily scale in this direction even up to square geometry since the supersite Hamiltonian Eq. (44) is local. As we write those parts of the tensor network to disk which are not involved in the local DMRG optimization, the influence of the system's width on memory consumption is constant. We found this to be around 1.8 TB for our maximum bond dimension of $m = 512$. Regarding the runtime, the scaling is linear as the MPO bond dimension is constant (∼80 for our benchmark), as we just need to update more supersites. A detailed discussion of the computational requirements can be found in Appendix D 3.

Energies and other operators with extensively scaling operator norms might be notoriously difficult observables for EE to match up to high numerical accuracy. For the chosen parameters of the 2D $U - V$ Hubbard Hamiltonian, at first glance the energies obtained seem to suggest the system to behave as effectively uncoupled 1D chains. Specifically, the isolated-chain ground state energy from DMRG is

$$E_{1D} = -12.022\,406\,40, \tag{45}$$

while the slope of the EE energy shown in Fig. 8 is

$$E_{EE}/W = -12.035\,131\,86 \pm 7.64 \times 10^{-6}. \tag{46}$$

To illustrate that we actually probe the 2D regime, we analyze chain-local quantities such as correlators. Concretely,

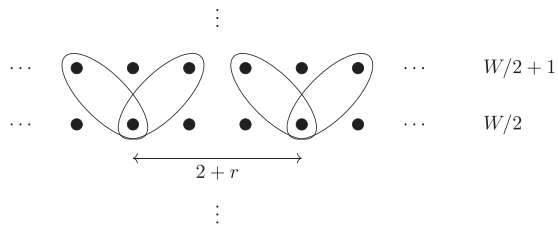


FIG. 9. Singlets on neighboring chains are connected by the d_{xy} correlator defined in Eq. (48).

we follow [62] in defining the nearest neighbor spin-singlet operators

$$\hat{D}_{x,y,a,b} = \hat{c}_{x,y,\uparrow}\hat{c}_{x+a,y+b,\downarrow} - \hat{c}_{x,y,\downarrow}\hat{c}_{x+a,y+b,\uparrow} \tag{47}$$

that connect the two central chains. From these, we build the d_{xy}-correlation function (c.f. Fig. 9), as this order has been identified as the most likely instability for these parameters in Ref. [62]

$$d_{xy}(r) = \langle\psi|(\hat{D}_{L/2+1,W/2,-1,1} - \hat{D}_{L/2+1,W/2,1,1})^\dagger \cdot (\hat{D}_{L/2+3+r,W/2,-1,1} - \hat{D}_{L/2+3+r,W/2,1,1})|\psi\rangle. \tag{48}$$

In evaluating this correlator in EE we need to multiply out all 16 terms in Eq. (48) and obtain operator strings which always consists of two creation and two annihilation operators.

The comparison between the EE-calculated result and the brute-force approach is shown in Fig. 10, for a system with $L = 20$. We see excellent agreement of the absolute values of the correlators in comparison to the pDMRG data, in particular given their small amplitudes. The strong enhancement to the short-range correlations of the d_{xy} singlets that is exclusive to $W \geqslant 4$ and which was described in [62] is a mark of the 2D nature of the model at these parameters. The EE-framework reproduces this effect with a small fraction of that computational effort.

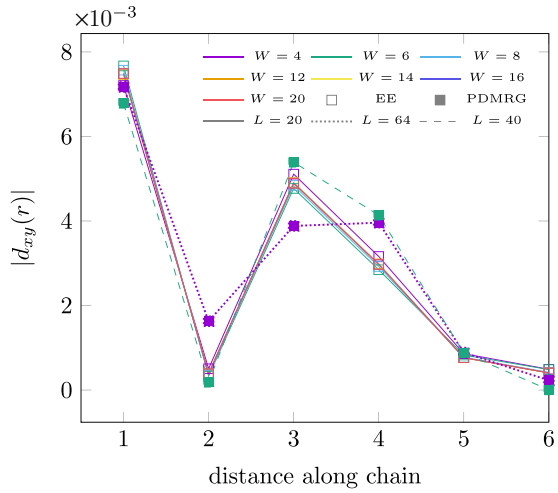


FIG. 10. d_{xy}-correlator for a 2D $U - V$ Hubbard model with $U/t = 4, V/t = 1$ at quarter filling $N = LW/2$, for different numbers of chains W, coupled with $t_\perp = 0.1$. EE-results for chains of length $L = 20$ (—) are compared to results computed using distributed-memory pDMRG for four or six chains of length $L = 64$ (- - - - - -) and $L = 40$ (- - -), respectively [62].

IV. CONCLUSION

The present work introduces a new many-body numerical algorithm for calculating the ground state of correlated 2D systems with spatial anisotropy. It exploits that modern MPS-based numerics can obtain a substantial number of the low-lying many-body eigenstates of the 1D subunits making up the systems, especially if symmetries are exploited. These states are then used to span the low-energy manifold of the full 2D system, within which a second DMRG algorithm is deployed to obtain the ground state. The EE-approach is thus able to efficiently exploit the spatial anisotropy, provided that the energy-spectrum spanned by the 1D basis sets is at least as wide as the effective coupling mediated by the interactions between the subunits. Where possible, we validate the algorithm either against QMC numerics (for hardcore bosons on the square lattice), or brute-force calculations carried out with distributed-memory DMRG (2D U-V Hubbard model at $N/L = 0.5$).

We demonstrate that the EE-approach can correctly detect the AFM emerging for localized spins on the anisotropic square lattice, as validated by QMC numerics. We then deploy the EE-framework to spins on the anisotropic triangular lattice, which has been studied intensely for its potential to realize spin liquids. Treating lattices of unprecedented size, we provide evidence for the existence of a gapless quasi-1D spin liquid in this model at the lowest couplings that we study. At the same time, our data appears to be at variance with earlier predictions that higher-order processes might stabilize an AFM at low coupling, or of a quantum phase transition occurring at intermediate transverse coupling. At present, we are precluded from studying the expected transition to spiral ordered phases by persistent convergence problems in the presence of finite fluxes. We also show the ability of the approach to treat repulsively interacting fermions away from integer filling for large systems that are not confined to narrow strips. Here, we demonstrate that the EE-technique can provide results of comparable quality to those obtained by brute-force approaches, but with far lower resource requirements.

At the technical level, the present work invites future studies into the cause for the persistent gaps—in those cases where they can be quantified—between the observables computed from the EE-approach and the true value of the observable, as can be seen, e.g., in Fig. 17. As the size of the 1D basis-set is increased, observables saturate to values that are generally different from their true value. We hypothesize that this persistent gap, which is small at the lower end of the system sizes and interchain couplings covered in this work and continuously grows from there, is caused either individually or collectively by the vast manifold of 1D basis states that fall below the user-defined cut-off, as discussed in Sec. II C. While each on their own may contribute only near-infinitesimally to an observable, the object of future work would be to quantify whether and how their exponentially growing number may result in an overall contribution that scales with system size and interchain coupling, as we find to be the case.

At present, the EE-framework as shown here has to deal with large intermediate memory-requirements. These are caused by the interplay of the contractions when building up

the Krylov subspace vectors in the standard formulation of the DMRG-algorithm, with the large local Hilbert-spaces spanned by the basis sets of the 1D subunits. For the larger systems for which we demonstrate the EE-approach here, this limits the deployment of the method to large-RAM machines at present. However, as discussed in Appendix D, there would be alternative versions of the DMRG algorithm that could trade an increase in computational time for a drastic decrease of the intermediate memory requirements.

Another aspect to be explored in future work would be the extension of the EE-framework to systems at finite temperatures or when evolving out-of-equilibrium. The most common way of deploying MPS-based techniques to finite temperatures, state purification, could be applied by the use of the TDVP-technique for imaginary time evolution, but METTS might also be an attractive possible alternative, given the potentially large local Hilbert spaces of our new method. Of course, computing finite-temperature properties within the EE-approach presupposes that the temperature would be small compared to the spread of energies covered by the 1D basis sets. Analogously, the study of out-of-equilibrium dynamics within the EE-framework would need to focus on processes that evolve slowly enough to be captured within the bandwidth of 1D basis states. Depending on the range of coupling in between 1D subunits, it could be carried out by running either a TEBD-algorithm for real time evolution (if coupling is strictly nearest-neighbor), or TDVP (if any of the couplings would be longer-ranged). If spectral functions related to perturbing operators $\hat{O}_{1,2}$ were desired, these could be obtained from the Fourier-transform of the matrix element $\langle\psi|e^{iE_{GS}t}\hat{O}_2 e^{-i\hat{H}t}\hat{O}_1|\psi\rangle$, where $\hat{H}$ and $|\psi\rangle$ represent the Hamiltonian and 2D wave function, as approximated by the EE-framework, respectively. Spectral functions could also be computed directly in frequency-space using $\hat{H}$ and $|\psi\rangle$, $\langle\psi|\hat{O}_2(\omega+i\eta-\hat{H})^{-1}\hat{O}_1|\psi\rangle$ as long as ω is significantly smaller than the spread of energies covered by the 1D-basis $|e\rangle$ [82].

Finally, another interesting line of future work would lie in comparing the EE-technique against other algorithms that can treat large correlated 2D-systems, but are not tailor-made for the spatially anisotropic regime, such as PEPS and phase-free or constrained-path AFQMC. In this setting, it can be difficult to estimate the degree of approximation induced by these methods and the EE-approach could serve to validate calculations with these alternative algorithms.

ACKNOWLEDGMENTS

S.M. and A.K. would like to thank Thierry Giamarchi for helpful discussions. This work was supported by an ERC Starting Grant from the European Union's Horizon 2020 research and innovation programme under Grant Agreement No. 758935; and the UK's Engineering and Physical Sciences Research Council [EPSRC; Grant No. EP/W022982/1]. J.M. acknowledges funding through SNSF Swiss Postdoctoral Fellowship, Grant No. 210478. The computations were enabled by resources provided through multiple EPSRC "Access to HPC" calls (Spring 2023, Autumn 2023, Spring 2024, and Autumn 2024) on the ARCHER2, Peta4-Skylake and Cirrus compute clusters, as well as by compute time awarded by the National Academic Infrastructure for Supercomputing in Sweden (NAISS). This work was supported by a grant from the Swiss National Supercomputing Centre (CSCS) under project ID s1307 on Alps. S.M. gratefully acknowledges the computing time provided on the high-performance computers noctua2 at the NHR Center PC2 in Paderborn. These are funded by the Federal Ministry of Education and Research and the state governments participating on the basis of the resolutions of the GWK for the national high performance computing at universities. All calculations were carried out with the publicly available containers of the SyTen toolkit [83]. N.L. acknowledges the ANR research Grant ManyBodyNet No. ANR-24-CE30-5851, the support of the Fondation Simone et Cino Del Duca, and the use of HPC resources from CALMIP (Grant No. 2023-P0677) and GENCI (Project No. A0150500225).

DATA AVAILABILITY

The data that support the findings of this article are not publicly available upon publication because it is not technically feasible and/or the cost of preparing, depositing, and hosting the data would be prohibitive within the terms of this research project. The data are available from the authors upon reasonable request.

APPENDIX A: EE-DMRG FINITE BOND DIMENSION ERROR

The error arising from finite bond dimension can be estimated used the truncated weight w, i.e., the sum of discarded singular values s_i

$$w = \sum_{i=m+1}^{M} s_i^2, \tag{A1}$$

where m is the number of states kept and M is the bond dimension before truncation. Often the truncated weight for the investigated model is constant for different parameter settings and therefore mentioned in the main text. For the systems discussed in Sec. III B it depends on the lattice geometry and coupling and therefore is displayed in Fig. 11.

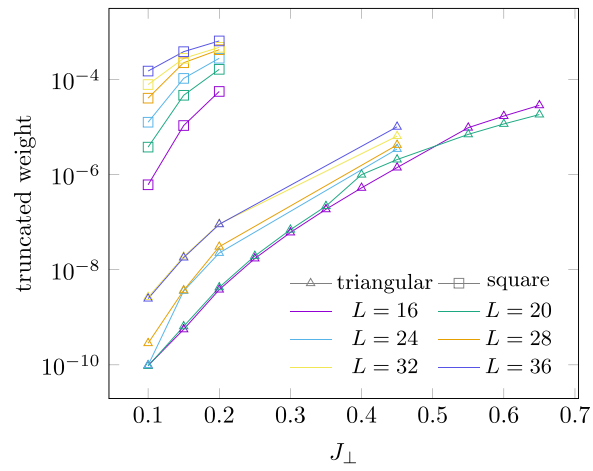


FIG. 11. Truncated weights for the final sweep of the different system sizes and intrachain couplings $J_\perp$ in Sec. III B.

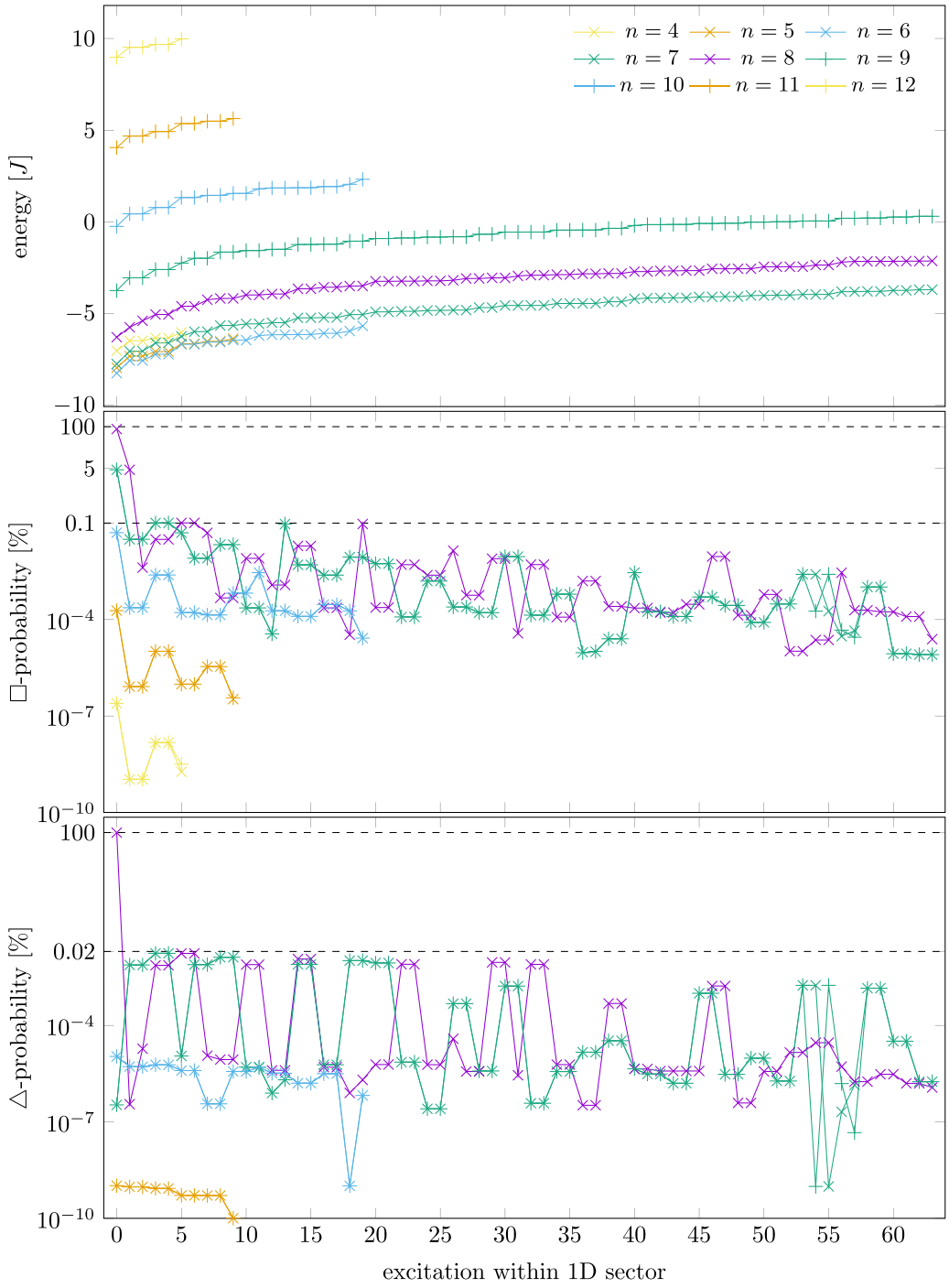


FIG. 12. Energy bandwidth of the 1D basis states and excitation probability in the center of the EE wave function for the system described in Eqs. (28) and (33). All data shown here is for chains of length $L = 16$ and in the center of a $W = 16$ supersites system with $J_\perp = 0.1$ and the local basis configuration described in Eq. (25). Changing the lattice geometry from square to triangular introduces frustration so efficient that the chains transition from a weakly coupled system to one of nearly independent chains, i.e., a product wave function of the 1D ground states.

APPENDIX B: SINGLE CHAIN EXCITATION PROBABILITIES

In order to estimate the importance of a particular chain energy mode within the 2D system, we plot the single chain excitation probability

$$\hat{\rho}_y = \mathrm{tr}_{y' \neq y} |\psi\rangle\langle\psi|. \tag{B1}$$

TABLE I. Single chain sectors incorporated in fermionic wave functions and their associated number of excitations. Note that some of the sectors might not be necessary as judged by the RDM, but still need to be included due to the creator (or annihilator) mapping from a state which has high enough weight to this low weight state. In this case, we added the ground state of this sector such that the block has size one and the irreducible representation is present in the wave function.

Particle number n	Spin $\lvert z\rvert$	1D states
$L/2-3$	$1/2$	$e=0$
$L/2-2$	$\leqslant 2$	$0\leqslant e\leqslant 9$
$L/2-1$	$5/2$	$e=0$
	$\leqslant 3/2$	$0\leqslant e\leqslant 15$
$L/2$	3	$e=0$
	$\leqslant 2$	$0\leqslant e\leqslant 19$
	0	$0\leqslant e\leqslant 31$
$L/2+1$	$7/2,\ 5/2$	$e=0$
	$\leqslant 3/2$	$0\leqslant e\leqslant 15$
$L/2+2$	$4,\ 3$	$e=0$
	$\leqslant 2$	$0\leqslant e\leqslant 9$
$L/2+3$	$3/2\leqslant \lvert z\rvert\leqslant 9/2$	$e=0$
	$1/2$	$0\leqslant e\leqslant 5$

We trace out everything except for the respective chain's energy eigenmodes. The diagonal elements of this matrix give us the excitation probability for the respective mode which can be seen in Fig. 12 together with the 1D energy bandwidth.

APPENDIX C: FERMIONIC 1D BASIS

Due to the fact that fermions have spin degeneracy for each particle number sector, we need to give a vector of 1D energy eigenstates kept in EE for each of those sectors. This scheme is depicted in Table I.

APPENDIX D: KEY ALGORITHMIC STEPS

1. 1D eigensystem

We obtain the 1D eigenbasis of the chain by using conventional DMRG [38]. DMRG has proven its utility and accuracy in efficiently computing eigenstates of 1D systems at high accuracy. Its performance stems from the small entanglement entropy of low-energy states scaling only very weakly with subsystem size in general. Once the ground state of the system $|e=0\rangle$ is found, we can compute low-lying excitations by minimizing the energy in DMRG with the additional constraint of orthogonality to all previously computed states [38].

$$\min_{|e\rangle}\left[\langle e|\hat{h}|e\rangle - E_e\langle e|e\rangle - \sum_{e'=0}^{e}\lambda_{e'}\langle e'|e'\rangle e\right]. \tag{D1}$$

Algorithmically, this consists in keeping the states against which the current excitation should be orthogonalized in the usual canonical form and computing their overlaps with the MPS site tensor in the local diagonalization step of DMRG. This part of the algorithm is shown in Fig. 13. Depending on the boundary conditions, the exact geometry of the 1D lattice, the Hamiltonian parameters and the exchange statistics of the particles, the typical bond dimension for convergence of such a state can range from $m\sim\mathcal{O}(100..1000)$. The typical MPS size on disk then reaches from below 1 MB to several hundreds. The calculation itself uses O(10 GB) of RAM and takes between minutes and hours. Since all lower-lying excitations are necessary to compute an excited state, there is no room for parallelization. However, in addition to the usual parallelization over tensor blocks we can search in the different quantum number sectors in parallel, as described in Sec. II A.

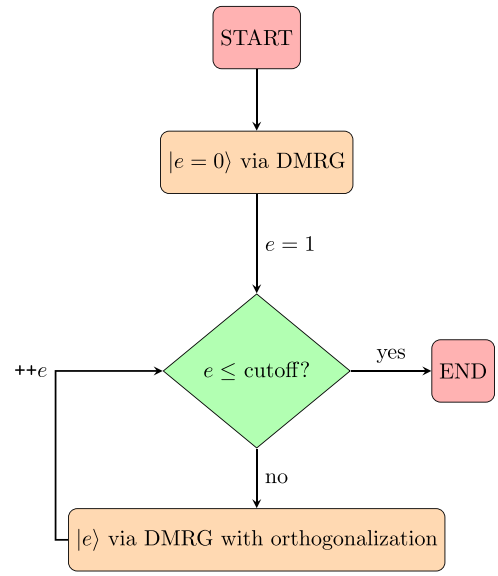


FIG. 13. Schematic depiction of the orthogonalization procedure to obtain the low lying excitations of the 1D Hamiltonian $\hat{H}_1$. Note that we can perform this scheme for each symmetry sector separately and thus in parallel.

2. Matrix elements

Once we have obtained a sufficient amount of 1D energy eigenstates to describe our system accurately, we need to extract the necessary matrix elements for the transformation of Eq. (1) into the 1D energy eigenbasis. For each state $|e,\sigma\rangle$ labeled by its sector σ and excitation number within that sector e, we need to compute the overlap with all the other states $\{|e',\sigma+T\rangle\}_{e'}$. Here, T is the transformation behavior of the operator—the change in quantum number(s) that applying it induces—that we are measuring and the target sector is $\sigma+T$. The whole scheme is depicted in Fig. 14. The typical size of these matrices is O(10) × O(10), i.e., the computational cost is negligible. The overlap performance on two MPSs typically needs less than 10 GB of RAM and under one minute. Again, we have the advantage that we can parallelize the computation over tensor blocks and, in addition to that, by computing all matrix elements in parallel since we do not have to wait for lower lying elements in the spectrum to finish.

3. EE-DMRG

Here, we describe the most costly computational step of the algorithm. Since our Hamiltonian represents each chain

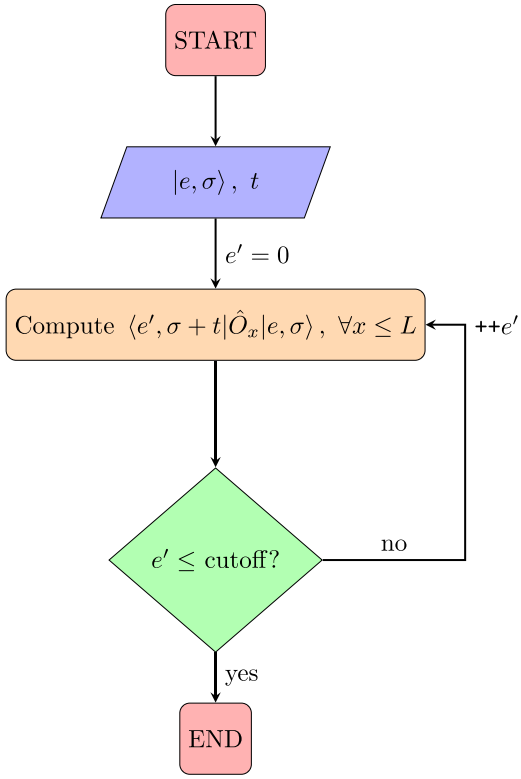


FIG. 14. Computing the matrix elements for the local operators needed in EE, typically $c_x^{(\dagger)}$ and n_x. For each operator and each eigenstate computed in 1D we need to compute the overlap with all eigenstates in the sector which we obtain by combining the original sector and the transformation behavior of the operator at hand. Note that we can do this in parallel for all states and all operators.

as a large effective supersite, the typical bond dimension of $\hat{H}_\perp$ is rather modest. However, the MPO bond dimension does scale with the length of the chains L, as the summation contains an element for each site x. We typically found a bond dimension $\mathcal{O}(10)$ for the systems investigated in this work ranging from ∼30 for bosons on the square lattice to ∼80 for spins on triangular lattices and the fermionic systems we looked at. Together with the bond dimension accessible to EE in two-site DMRG, this typically resulted in sizes of the left-and right-environments being $\mathcal{O}(100\,\mathrm{MB})$. Furthermore, the MPS tensors themselves would have a size of the order $\mathcal{O}(10\,\mathrm{MB}..50\,\mathrm{MB})$. We define the filling fraction of a tensor as the ratio between the amount of memory needed when the tensor is symmetry protected [4] compared to a the hypothetical total amount of memory necessary would one want to store the object without blocks. This yields a filling fraction of ∼17% for the MPS site tensors. Using the same filling fraction to compute the size of the objects computed in Fig. 15, we arrive at around 500 GB just to store the partial contractions in RAM. We note that the filling fraction is usually not a constant throughout a tensor network and hence the objects might actually be larger. However, the magnitude matches the memory consumption experienced by us during simulations. Upon multiplication of the site tensor into the left boundary the memory requirement for performing the further multiplications of a state with bond dimension $m = 256$ jumps to 2 TB. With the highest-RAM machines available to us, we were able to perform this calculation, as we cache the other elements of the tensor network not needed for the local update to disk.

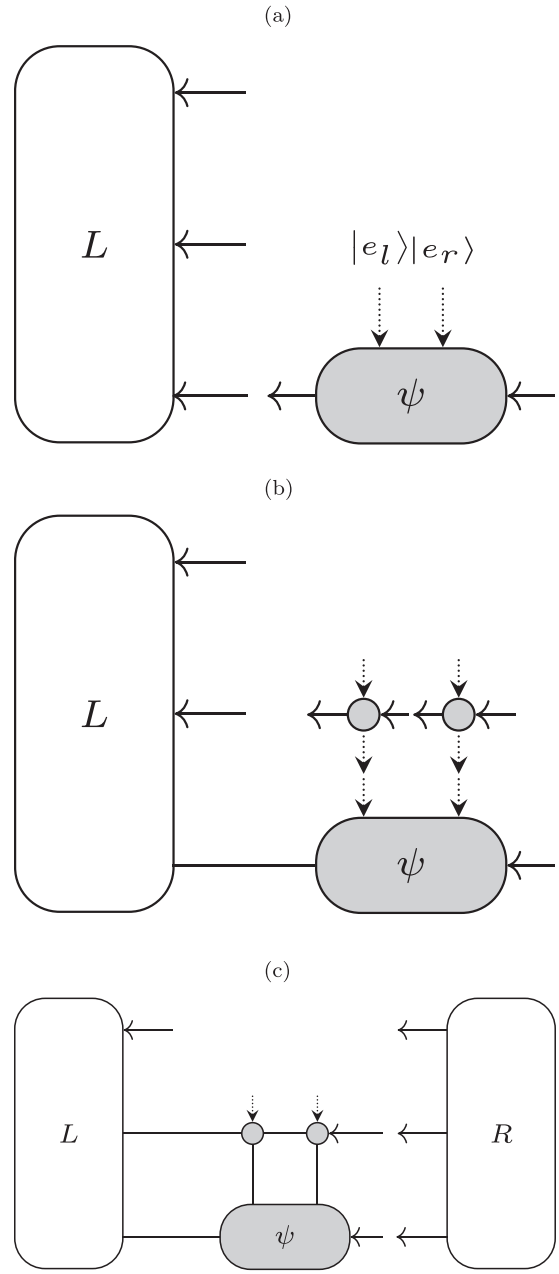


FIG. 15. Key algorithmic steps of the local two-site update in EE-DMRG. (a) Applying the active two-site tensor to the left environment. This step greatly increases memory usage due to two open legs with large local Hilbert space $\tilde{d}$ size and an additional free MPO leg. (b) Applying the MPO site tensors to the composite object. This step still involves the high RAM requirement as the number of open legs remains the same and we contract with objects scaling as $\tilde{d}$ and the MPO bond dimension. (c) Finally, this step gives us the updated MPS tensor and the memory requirement again drops to the well controllable amounts described in the main text.

There are two potential remedies for the high-RAM requirements. We outline these here, but pursuing them in detail would constitute a separate project. The first is the use of

single-site DMRG instead of two-site optimization [84]. The advantage of the single-site approach is that it requires only a single index running over the 1D basis states, of size $\tilde{d}$, during the optimization approach in Fig. 15, instead of the two indices, each of size $\tilde{d}$, for two-site DMRG. For instance, a test calculation performed on the system in Sec. III B yielded a decreased RAM consumption by a factor of ten while keeping the bond dimension constant. Given that we use $\tilde{d} = 264$ single-chain basis states in production, this is an appropriate improvement. In order to improve accuracy, we then increase bond dimension within the single-site DMRG algorithm up to $m = 1024$, where our original RAM restriction of 2 TB kicks in. However, systems with weak interchain coupling would often converge around bond dimensions of about $m = 500$ and not saturate the available number of states, in particular for $J_\perp < 0.5$. The improved performance of single-site DMRG, however, entails potential problems regarding the convergence of the wave function. Usually, single site DMRG can run into convergence problems due to the limited size of the local variational Hilbert space available during the application. Algorithms exist that attempt to mitigate this by mixing the optimized state tensor with additional data, such that the algorithm might be able to explore a larger variational manifold [84]. The truncation then automatically takes care of unnecessary degrees of freedom. However, there is no guarantee for the expansion data to actually contain the necessary states for the MPS to reach a true minimum in the energy optimization landscape. Running these codes thus entails a case by case decision on whether single-site DMRG has found a state that converged equally well or even better than the one found by two-site DMRG with fewer resources, or whether one might be stuck in a metastable state. Within the EE-framework as deployed in the present work, there is the advantage that all supersite "interactions" are either local or at most nearest-neighbor. Hence, the single-site DMRG might not be obstructed by long range interactions, which is a fairly common problem for this algorithm. For the triangular test systems the difference between single-site and two-site energies would be around $10^{-2}\%$, with the single site DMRG being lower in energy. Key observables, e.g., the correlators in Fig. 5, would take exactly the same shape. This overlap between both results indicates the correctness of our results obtained with finite bond dimension. However, employing single-site DMRG for data production, we would consider additional checks to be necessary that will be the target for future work.

The second possible mitigation to the resource problem might be introducing an additional step during the two-site update, which is shown in Fig. 15 for reference. If we want to avoid the occurrence of objects with two supersite indices, each having a local dimension of $\tilde{d}$, we could compute the contraction of the left environment, the left MPS and the left local MPO tensor separately from the analogous contractions for the right-sided objects. The updated two-site tensor would then be computed from contracting the left-side and the right-side network. Furthermore, left-side and right-side network would need to be kept separate consistently as the Krylov subspace is being built up by subsequent applications of the Hamiltonian. This necessitates application of a QR decomposition for every two-site tensor (i.e., after every application of the Hamiltonian). By doing so, the memory cost would stay comparable to that of single-site DMRG, but at the cost of additional QRs at every update step. Trading memory for compute time in this fashion would allow keeping the large variational Hilbert space of the two-site procedure and hence avoid potential local minima. Based on pilot results, we currently estimate a runtime that would be four to five times longer than that of the standard algorithm used in the present work.

APPENDIX E: ENERGY EIGENSTATE OBSERVABLE OVERLAPS

As discussed in Sec. II B, observables computed with EE wave functions are summations over the 1D matrix elements of $\hat{H}_1$ weighted by the RDM of the corresponding chain supersite Hilbert spaces. Here, we want to demonstrate the spatial behavior of these matrix elements. For instance, in order to compute the single-particle density matrix of the system described in Sec. III A, we must expand

$$\langle\psi|\hat{b}^\dagger_{xc}\hat{b}_{x'c}|\psi\rangle = \sum_{n_y e_y e'_y} \rho^{n_y e'_y}_{n_y e_y} \langle ne|\hat{b}^\dagger_x \hat{b}_{x'}|ne'\rangle_c, \tag{E1}$$

where we introduced the single chain RDM

$$\rho^{n_y e'_y}_{n_y e_y} = M^{n_y e_y \dagger} \cdot M^{n_y e'_y} \tag{E2}$$

and $c = W/2$ again. We are now particularly interested in the 1D matrix elements of different eigenstates $|e\rangle$ and $|e'\rangle$ of $\hat{H}_1$. In the case of $e \neq e'$ these are not observables themselves but their scaling is crucial for the EE to be able to capture 2D physics such as off-diagonal long range order correctly. The results for the system of size $L = 16$ at half filling $N = 8$ and chain nearest neighbor repulsion $V = 2$ are shown in Fig. 16.

APPENDIX F: OBSERVABLE SCALING WITH SUPERSITE SIZE

The number of 1D states incorporated into the local supersite is crucial for the convergence of many observables and the quantum state $|\psi\rangle$ itself. Here we want to demonstrate the impact that different values of the dimension $\tilde{d}$ of the retained single-chain Hilbert space can have on the square-lattice spin system discussed in Sec. III B. As QMC does not suffer from the sign problem for this model, we can validate convergence of the EE framework against data that is exact for all practical purposes. The definition of the perpendicular spin-spin correlator is given in Eqs. (31) and (32). We emphasize that $\tilde{d}$ does not uniquely specify a basis, as one 1D state removed from one sector while another one is being added to another sector will not change the value of $\tilde{d}$. In addition, we introduce the distance of two states $|\psi\rangle$ and $|\tilde{\psi}\rangle$ as

$$f(|\psi\rangle, |\tilde{\psi}\rangle) = \||\psi\rangle - |\tilde{\psi}\rangle\|_2^2, \tag{F1}$$

as a measure how much a state with large supersite Hilbert space $|\psi\rangle$ is varying from a state with a smaller supersite Hilbert space. The relative error of the results compared to exact QMC data is shown in Fig. 17 for the anisotropic Heisenberg Hamiltonian on the square lattice (c.f. Sec. III B). All results were obtained for a final bond dimension of

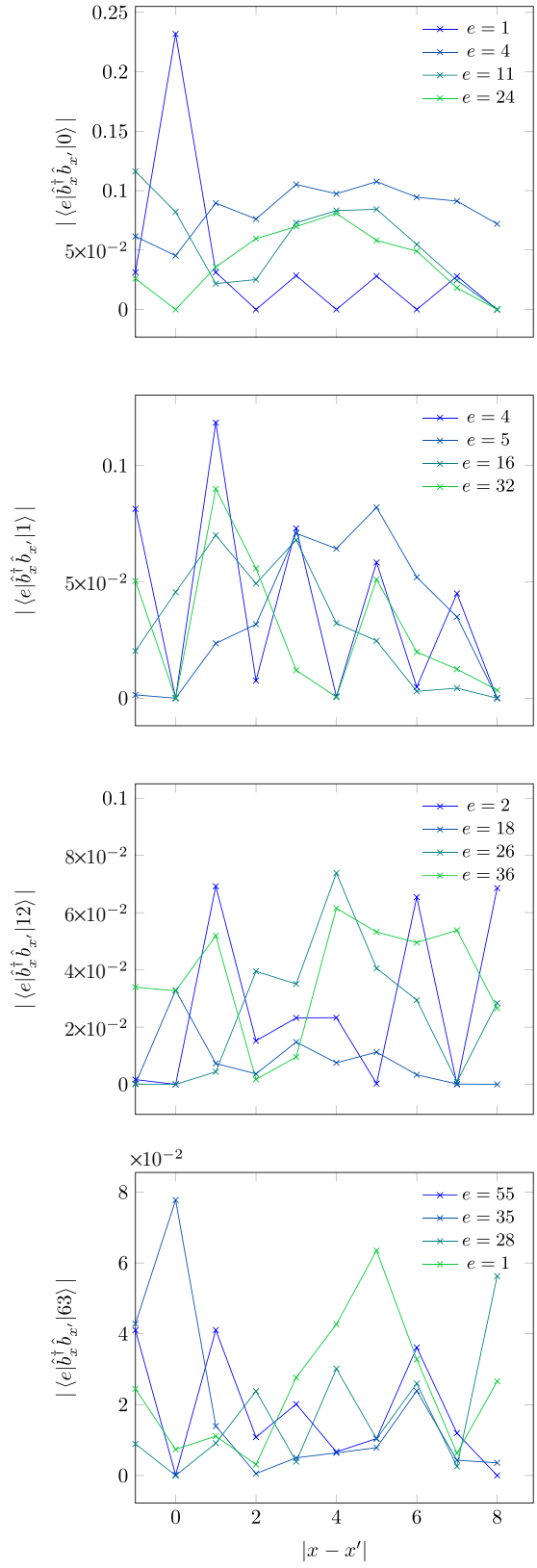


FIG. 16. 1D single particle correlation functions for $N = 8$ HCBs on a $L = 16$ chain with $V = 2$. The excited states with which the correlator was computed were manually picked to show functions which would not decay towards zero and hence could mimic the true 2D behavior in the weighted sum Eq. (E1).

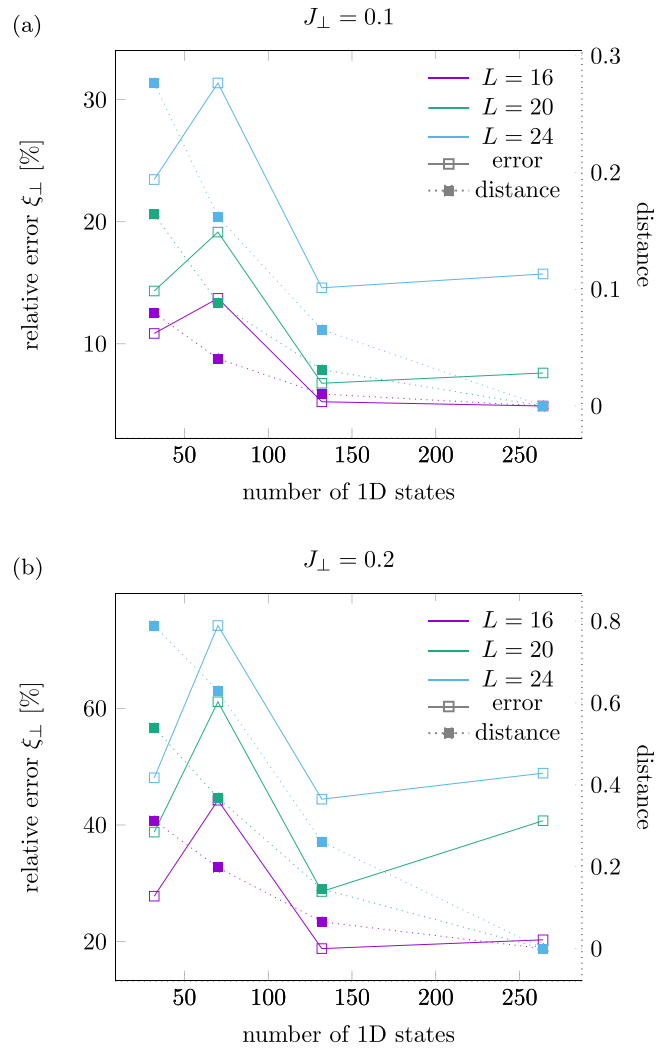


FIG. 17. Relative error of perpendicular correlation length defined in Eq. (32) for the square lattice (□) spin system defined in Eq. (28) compared to exact QMC. The right y axis shows the distance of the quantum states relative to the state with the largest local basis using dotted lines (- - - - - -).

$m = 256$ to maintain comparability, even though the smaller Hilbert space sizes can be computed with higher bond dimension. We clearly recognize the distance to be a monotonically decreasing function in $\tilde{d}$ while the same does not hold for the correlation length $\xi_\perp$. This is most likely due to higher bond dimension necessary to resolve correlations when more chain eigenstates are involved in the process.

APPENDIX G: SPIN TO HARDCORE BOSON MAPPING

Starting from Eq. (27) and identifying spin down with an empty and spin up with an occupied site we arrive at the hardcore boson Hamiltonians

$$2H_1 = \sum_{xy} (\hat{b}^\dagger_{x,y}\hat{b}_{x+1,y} + \hat{b}^\dagger_{x+1,y}\hat{b}_{x,y}) + 2/t \sum_{xy} \hat{n}_{x,y}\hat{n}_{x+1,y} + \text{const.}, \quad \text{(G1)}$$

$$2H_\perp = \sum_{xy} (\hat{b}^\dagger_{x,y}\hat{b}_{x,y+1} + \hat{b}^\dagger_{x,y+1}\hat{b}_{x,y}) + 2/t \sum_{xy} \hat{n}_{x,y}\hat{n}_{x,y+1} + \text{const.}, \quad \text{(G2)}$$

$$2H'_\perp = \sum_{xy} (\hat{b}^\dagger_{x,y}\hat{b}_{x+1,y+1} + \hat{b}^\dagger_{x+1,y+1}\hat{b}_{x,y}) + 2/t \sum_{xy} \hat{n}_{x,y}\hat{n}_{x+1,y+1} + \text{const.}, \quad \text{(G3)}$$

where we introduced the ordinary creation and annihilation operators as well as the particle number operator. This means the two models are essentially the same with the identifications

$$t = J, \quad V = 2J, \quad t_\perp = J_\perp, \quad V_\perp = 2J_\perp. \quad \text{(G4)}$$

It is worthwhile pointing out that the sign of the HCB kinetic energy is positive now in all three Eqs. (G1)–(G3) which shifts the energy minimum of the single particle dispersion from zero momentum to $(\pi/a, \pi/a)$.

[1] C. Bourbonnais and D. Jérome, Interacting electrons in quasi-one-dimensional organic superconductors, in *The Physics of Organic Superconductors and Conductors*, edited by A. Lebed (Springer, Heidelberg, 2008), p. 357.

[2] D. Jerome and C. Bourbonnais, Quasi one-dimensional organic conductors: From Fröhlich conductivity and Peierls insulating state to magnetically-mediated superconductivity, a retrospective, C. R. Phys. **25**, 17 (2024).

[3] T. Nagata, M. Uehara, J. Goto, J. Akimitsu, N. Motoyama, H. Eisaki, S. Uchida, H. Takahashi, T. Nakanishi, and N. Môri, Pressure-Induced dimensional crossover and superconductivity in the hole-doped two-leg ladder compound $Sr_{14-x}Ca_xCu_{24}O_{41}$, Phys. Rev. Lett. **81**, 1090 (1998).

[4] E. Dagotto, Experiments on ladders reveal a complex interplay between a spin-gapped normal state and superconductivity, Rep. Prog. Phys. **62**, 1525 (1999).

[5] J.-K. Bao, J.-Y. Liu, C.-W. Ma, Z.-H. Meng, Z.-T. Tang, Y.-L. Sun, H.-F. Zhai, H. Jiang, H. Bai, C.-M. Feng, Z.-A. Xu, and G.-H. Cao, Superconductivity in quasi-one-dimensional $K_2Cr_3As_3$ with significant electron correlations, Phys. Rev. X **5**, 011013 (2015).

[6] M. D. Watson, Y. Feng, C. W. Nicholson, C. Monney, J. M. Riley, H. Iwasawa, K. Refson, V. Sacksteder, D. T. Adroja, J. Zhao, and M. Hoesch, Multiband one-dimensional electronic structure and spectroscopic signature of Tomonaga-Luttinger liquid behavior in $K_2Cr_3As_3$, Phys. Rev. Lett. **118**, 097002 (2017).

[7] R. Coldea, D. A. Tennant, R. A. Cowley, D. F. McMorrow, B. Dorner, and Z. Tylczynski, Neutron scattering study of the magnetic structure of Cs_2CuCl_4, J. Phys.: Condens. Matter **8**, 7473 (1996).

[8] R. Coldea, D. A. Tennant, A. M. Tsvelik, and Z. Tylczynski, Experimental realization of a 2D fractional quantum spin liquid, Phys. Rev. Lett. **86**, 1335 (2001).

[9] R. Coldea, D. A. Tennant, K. Habicht, P. Smeibidl, C. Wolters, and Z. Tylczynski, Direct measurement of the spin Hamiltonian and observation of condensation of magnons in the 2D frustrated quantum magnet Cs_2CuCl_4, Phys. Rev. Lett. **88**, 137203 (2002).

[10] H. Tanaka, T. Ono, H. A. Katori, H. Mitamura, F. Ishikawa, and T. Goto, Magnetic phase transition and magnetization plateau in Cs_2CuBr_4, Prog. Theor. Phys. Suppl. **145**, 101 (2002).

[11] T. Ono, H. Tanaka, H. Aruga Katori, F. Ishikawa, H. Mitamura, and T. Goto, Magnetization plateau in the frustrated quantum spin system Cs_2CuBr_4, Phys. Rev. B **67**, 104431 (2003).

[12] J. Alicea, O. I. Motrunich, and M. P. A. Fisher, Theory of the algebraic vortex liquid in an anisotropic spin-$\frac{1}{2}$ triangular antiferromagnet, Phys. Rev. B **73**, 174430 (2006).

[13] M. Q. Weng, D. N. Sheng, Z. Y. Weng, and R. J. Bursill, Spin-liquid phase in an anisotropic triangular-lattice Heisenberg model: Exact diagonalization and density-matrix renormalization group calculations, Phys. Rev. B **74**, 012407 (2006).

[14] S. Yunoki and S. Sorella, Two spin liquid phases in the spatially anisotropic triangular Heisenberg model, Phys. Rev. B **74**, 014408 (2006).

[15] J. O. Fjærestad, W. Zheng, R. R. P. Singh, R. H. McKenzie, and R. Coldea, Excitation spectra and ground state properties of the layered spin-$\frac{1}{2}$ frustrated antiferromagnets Cs_2CuCl_4 and Cs_2CuBr_4, Phys. Rev. B **75**, 174447 (2007).

[16] O. A. Starykh and L. Balents, Ordering in spatially anisotropic triangular antiferromagnets, Phys. Rev. Lett. **98**, 077205 (2007).

[17] Y. Hayashi and M. Ogata, Possibility of gapless spin liquid state by one-dimensionalization, J. Phys. Soc. Jpn. **76**, 053705 (2007).

[18] T. Pardini and R. R. P. Singh, Magnetic order in coupled spin-half and spin-one Heisenberg chains in anisotropic triangular-lattice geometry, Phys. Rev. B **77**, 214433 (2008).

[19] D. Heidarian, S. Sorella, and F. Becca, Spin-$\frac{1}{2}$ Heisenberg model on the anisotropic triangular lattice: From magnetism to a one-dimensional spin liquid, Phys. Rev. B **80**, 012404 (2009).

[20] O. A. Starykh, H. Katsura, and L. Balents, Extreme sensitivity of a frustrated quantum magnet: Cs_2CuCl_4, Phys. Rev. B **82**, 014421 (2010).

[21] P. T. Cong, B. Wolf, M. de Souza, N. Krüger, A. A. Haghighirad, S. Gottlieb-Schoenmeyer, F. Ritter, W. Assmus, I. Opahle, K. Foyevtsova, H. O. Jeschke, R. Valentí, L. Wiehl, and M. Lang, Distinct magnetic regimes through site-selective atom substitution in the frustrated quantum antiferromagnet $Cs_2CuCl_{4-x}Br_x$, Phys. Rev. B **83**, 064425 (2011).

[22] A. Weichselbaum and S. R. White, Incommensurate correlations in the anisotropic triangular Heisenberg lattice, Phys. Rev. B **84**, 245130 (2011).

[23] J. Reuther and R. Thomale, Functional renormalization group for the anisotropic triangular antiferromagnet, Phys. Rev. B **83**, 024402 (2011).

[24] M. Thesberg and E. S. Sørensen, Exact diagonalization study of the anisotropic triangular lattice Heisenberg model using twisted boundary conditions, Phys. Rev. B **90**, 115117 (2014).

[25] E. Ghorbani, L. F. Tocchio, and F. Becca, Variational wave functions for the $s = \frac{1}{2}$ Heisenberg model on the anisotropic

triangular lattice: Spin liquids and spiral orders, Phys. Rev. B **93**, 085111 (2016).

[26] U. Tutsch, O. Tsyplyatyev, M. Kuhnt, L. Postulka, B. Wolf, P. T. Cong, F. Ritter, C. Krellner, W. Aßmus, B. Schmidt, P. Thalmeier, P. Kopietz, and M. Lang, Specific heat study of 1D and 2D excitations in the layered frustrated quantum antiferromagnets $Cs_2CuCl_{4-x}Br_x$, Phys. Rev. Lett. **123**, 147202 (2019).

[27] M. G. Gonzalez, E. A. Ghioldi, C. J. Gazza, L. O. Manuel, and A. E. Trumper, Interplay between spatial anisotropy and next-nearest-neighbor exchange interactions in the triangular Heisenberg model, Phys. Rev. B **102**, 224410 (2020).

[28] A. Szasz and J. Motruk, Phase diagram of the anisotropic triangular lattice Hubbard model, Phys. Rev. B **103**, 235132 (2021).

[29] M. Gonzalez, B. Bernu, L. Pierre, and L. Messio, Ground-state and thermodynamic properties of the spin-$\frac{1}{2}$ Heisenberg model on the anisotropic triangular lattice, SciPost Phys. **12**, 112 (2022).

[30] Y. Yu, S. Li, S. Iskakov, and E. Gull, Magnetic phases of the anisotropic triangular lattice Hubbard model, Phys. Rev. B **107**, 075106 (2023).

[31] P. W. Anderson, Physics of the pseudogap phase of high T_c cuprates, or, RVB meets umklapp, J. Phys. Chem. Solids **63**, 2145 (2002).

[32] D. J. Scalapino, A common thread: The pairing interaction for unconventional superconductors, Rev. Mod. Phys. **84**, 1383 (2012).

[33] G. R. Stewart, Unconventional superconductivity, Adv. Phys. **66**, 75 (2017).

[34] Y. Shimizu, K. Miyagawa, K. Kanoda, M. Maesato, and G. Saito, Spin liquid state in an organic Mott insulator with triangular lattice, Phys. Rev. Lett. **91**, 107001 (2003).

[35] T. Itou, A. Oyamada, S. Maegawa, M. Tamura, and R. Kato, Quantum spin liquid in the spin-$\frac{1}{2}$ triangular antiferromagnet $EtMe_3Sb[Pd(dmit)_2]_2$, Phys. Rev. B **77**, 104413 (2008).

[36] T. Itou, A. Oyamada, S. Maegawa, M. Tamura, and R. Kato, ^{13}C NMR study of the spin-liquid state in the triangular quantum antiferromagnet $EtMe_3Sb[Pd(dmit)_2]_2$, J. Phys.: Conf. Ser. **145**, 012039 (2009).

[37] T. Giamarchi, *Quantum Physics in One Dimension* (Oxford University Press, Oxford, 2003).

[38] U. Schollwöck, The density-matrix renormalization group in the age of matrix product states, Ann. Phys. **326**, 96 (2011).

[39] S. Paeckel, T. Köhler, A. Swoboda, S. R. Manmana, U. Schollwöck, and C. Hubig, Time-evolution methods for matrix-product states, Ann. Phys. **411**, 167998 (2019).

[40] H. J. Schulz, Dynamics of coupled quantum spin chains, Phys. Rev. Lett. **77**, 2790 (1996).

[41] T. Giamarchi and A. M. Tsvelik, Coupled ladders in a magnetic field, Phys. Rev. B **59**, 11398 (1999).

[42] A. W. Sandvik, Multichain mean-field theory of quasi-one-dimensional quantum spin systems, Phys. Rev. Lett. **83**, 3069 (1999).

[43] M. Dupont, S. Capponi, N. Laflorencie, and E. Orignac, Dynamical response and dimensional crossover for spatially anisotropic antiferromagnets, Phys. Rev. B **98**, 094403 (2018).

[44] G. Karakonstantakis, E. Berg, S. R. White, and S. A. Kivelson, Enhanced pairing in the checkerboard Hubbard ladder, Phys. Rev. B **83**, 054508 (2011).

[45] G. Bollmark, T. Köhler, L. Pizzino, Y. Yang, J. S. Hofmann, H. Shi, S. Zhang, T. Giamarchi, and A. Kantian, Solving 2D and 3D lattice models of correlated fermions—combining matrix product states with mean-field theory, Phys. Rev. X **13**, 011039 (2023).

[46] G. Bollmark, T. Köhler, and A. Kantian, Resolving competition of charge density wave and superconducting phases using the matrix product state plus mean field algorithm, Phys. Rev. B **111**, 125141 (2025).

[47] C. Rüegg, K. Kiefer, B. Thielemann, D. F. McMorrow, V. Zapf, B. Normand, M. B. Zvonarev, P. Bouillot, C. Kollath, T. Giamarchi, S. Capponi, D. Poilblanc, D. Biner, and K. W. Krämer, Thermodynamics of the spin Luttinger liquid in a model ladder material, Phys. Rev. Lett. **101**, 247202 (2008).

[48] M. Klanjšek, H. Mayaffre, C. Berthier, M. Horvatić, B. Chiari, O. Piovesana, P. Bouillot, C. Kollath, E. Orignac, R. Citro, and T. Giamarchi, Controlling Luttinger liquid physics in spin ladders under a magnetic field, Phys. Rev. Lett. **101**, 137207 (2008).

[49] B. Thielemann, C. Rüegg, K. Kiefer, H. M. Rønnow, B. Normand, P. Bouillot, C. Kollath, E. Orignac, R. Citro, T. Giamarchi, A. M. Läuchli, D. Biner, K. W. Krämer, F. Wolff-Fabris, V. S. Zapf, M. Jaime, J. Stahn, N. B. Christensen, B. Grenier, D. F. McMorrow *et al.*, Field-controlled magnetic order in the quantum spin-ladder system $(Hpip)_2CuBr_4$, Phys. Rev. B **79**, 020408(R) (2009).

[50] P. Bouillot, C. Kollath, A. M. Läuchli, M. Zvonarev, B. Thielemann, C. Rüegg, E. Orignac, R. Citro, M. Klanjšek, C. Berthier, M. Horvatić, and T. Giamarchi, Statics and dynamics of weakly coupled antiferromagnetic spin-$\frac{1}{2}$ ladders in a magnetic field, Phys. Rev. B **83**, 054407 (2011).

[51] G. Bollmark, N. Laflorencie, and A. Kantian, Dimensional crossover and phase transitions in coupled chains : Density matrix renormalization group results, Phys. Rev. B **102**, 195145 (2020).

[52] M. Jeong, H. Mayaffre, C. Berthier, D. Schmidiger, A. Zheludev, and M. Horvatić, Magnetic-order crossover in coupled spin ladders, Phys. Rev. Lett. **118**, 167206 (2017).

[53] D. Schmidiger, P. Bouillot, S. Mühlbauer, S. Gvasaliya, C. Kollath, T. Giamarchi, and A. Zheludev, Spectral and thermodynamic properties of a strong-leg quantum spin ladder, Phys. Rev. Lett. **108**, 167201 (2012).

[54] M. Jeong, H. Mayaffre, C. Berthier, D. Schmidiger, A. Zheludev, and M. Horvatić, Attractive Tomonaga-Luttinger liquid in a quantum spin ladder, Phys. Rev. Lett. **111**, 106404 (2013).

[55] S. C. Furuya, M. Dupont, S. Capponi, N. Laflorencie, and T. Giamarchi, Dimensional modulation of spontaneous magnetic order in quasi-two-dimensional quantum antiferromagnets, Phys. Rev. B **94**, 144403 (2016).

[56] S. Mukhopadhyay, M. Klanjšek, M. S. Grbić, R. Blinder, H. Mayaffre, C. Berthier, M. Horvatić, M. A. Continentino, A. Paduan-Filho, B. Chiari, and O. Piovesana, Quantum-critical spin dynamics in quasi-one-dimensional antiferromagnets, Phys. Rev. Lett. **109**, 177206 (2012).

[57] R. Blinder, M. Dupont, S. Mukhopadhyay, M. S. Grbić, N. Laflorencie, S. Capponi, H. Mayaffre, C. Berthier, A. Paduan-Filho, and M. Horvatić, Nuclear magnetic resonance study of the magnetic-field-induced ordered phase in the $NiCl_2$-4SC$(NH_2)_2$ compound, Phys. Rev. B **95**, 020404(R) (2017).

[58] S. Biermann, A. Georges, A. Lichtenstein, and T. Giamarchi, Deconfinement transition and Luttinger to Fermi liquid crossover in quasi-one-dimensional systems, Phys. Rev. Lett. **87**, 276405 (2001).

[59] C. Berthod, T. Giamarchi, S. Biermann, and A. Georges, Breakup of the Fermi surface near the Mott transition in low-dimensional systems, Phys. Rev. Lett. **97**, 136401 (2006).

[60] J. Eisert, M. Cramer, and M. B. Plenio, Colloquium: Area laws for the entanglement entropy, Rev. Mod. Phys. **82**, 277 (2010).

[61] E. Stoudenmire and S. R. White, Studying two-dimensional systems with the density matrix renormalization group, Annu. Rev. Condens. Matter Phys. **3**, 111 (2012).

[62] A. Kantian, M. Dolfi, M. Troyer, and T. Giamarchi, Understanding repulsively mediated superconductivity of correlated electrons via massively parallel density matrix renormalization group, Phys. Rev. B **100**, 075138 (2019).

[63] A. W. Sandvik, Computational studies of quantum spin systems, AIP Conf. Proc. **1297**, 135 (2010).

[64] A. M. Läuchli, Numerical simulations of frustrated systems, in *Introduction to Frustrated Magnetism: Materials, Experiments, Theory* (Springer, 2010), pp. 481–511.

[65] B. Bauer, L. D. Carr, H. G. Evertz, A. Feiguin, J. Freire, S. Fuchs, L. Gamper, J. Gukelberger, E. Gull, S. Guertler, A. Hehn, R. Igarashi, S. V. Isakov, D. Koop, P. N. Ma, P. Mates, H. Matsuo, O. Parcollet, G. Pawlowski, J. D. Picon *et al.*, The ALPS project release 2.0: Open source software for strongly correlated systems, J. Stat. Mech. (2011) P05001.

[66] A. Gaenko, A. Antipov, G. Carcassi, T. Chen, X. Chen, Q. Dong, L. Gamper, J. Gukelberger, R. Igarashi, S. Iskakov, M. Könz, J. LeBlanc, R. Levy, P. Ma, J. Paki, H. Shinaoka, S. Todo, M. Troyer, and E. Gull, Updated core libraries of the ALPS project, Comput. Phys. Commun. **213**, 235 (2017).

[67] F. Becca and S. Sorella, *Quantum Monte Carlo Approaches for Correlated Systems* (Cambridge University Press, 2017).

[68] J. I. Cirac, D. Pérez-García, N. Schuch, and F. Verstraete, Matrix product states and projected entangled pair states: Concepts, symmetries, theorems, Rev. Mod. Phys. **93**, 045003 (2021).

[69] Y. Y. He, M. Qin, H. Shi, Z. Y. Lu, and S. Zhang, Finite-temperature auxiliary-field quantum Monte Carlo: Self-consistent constraint and systematic approach to low temperatures, Phys. Rev. B **99**, 045108 (2019).

[70] A. J. A. James and R. M. Konik, Understanding the entanglement entropy and spectra of 2D quantum systems through arrays of coupled 1D chains, Phys. Rev. B **87**, 241103(R) (2013).

[71] A. J. A. James, R. M. Konik, P. Lecheminant, N. J. Robinson, and A. M. Tsvelik, Non-perturbative methodologies for low-dimensional strongly-correlated systems: From non-Abelian bosonization to truncated spectrum methods, Rep. Prog. Phys. **81**, 046002 (2018).

[72] G. Vidal, J. I. Latorre, E. Rico, and A. Kitaev, Entanglement in quantum critical phenomena, Phys. Rev. Lett. **90**, 227902 (2003).

[73] P. Calabrese and J. Cardy, Entanglement entropy and quantum field theory, J. Stat. Mech. (2004) P06002.

[74] C. Hubig, Symmetry-protected tensor networks, Dissertation, LMU Munich, 2017.

[75] S. Singh, R. N. C. Pfeifer, and G. Vidal, Tensor network decompositions in the presence of a global symmetry, Phys. Rev. A **82**, 050301(R) (2010).

[76] S. Singh, R. N. C. Pfeifer, and G. Vidal, Tensor network states and algorithms in the presence of a global U(1) symmetry, Phys. Rev. B **83**, 115125 (2011).

[77] U. Schollwöck, The density-matrix renormalization group, Rev. Mod. Phys. **77**, 259 (2005).

[78] O. F. Syljuåsen and A. W. Sandvik, Quantum Monte Carlo with directed loops, Phys. Rev. E **66**, 046701 (2002).

[79] Z. Weihong, R. H. McKenzie, and R. R. P. Singh, Phase diagram for a class of spin-half Heisenberg models interpolating between the square-lattice, the triangular-lattice and the linear chain limits, Phys. Rev. B **59**, 14367 (1999).

[80] C. Bourbonnais and A. Sedeki, Superconductivity and antiferromagnetism as interfering orders in organic conductors, C. R. Phys. **12**, 532 (2011).

[81] M. Qin, C.-M. Chung, H. Shi, E. Vitali, C. Hubig, U. Schollwöck, S. R. White, and S. Zhang (Simons Collaboration on the Many-Electron Problem), Absence of superconductivity in the pure two-dimensional Hubbard model, Phys. Rev. X **10**, 031016 (2020).

[82] A. Holzner, A. Weichselbaum, I. P. McCulloch, U. Schollwöck, and J. von Delft, Chebyshev matrix product state approach for spectral functions, Phys. Rev. B **83**, 195115 (2011).

[83] C. Hubig, F. Lachenmaier, N.-O. Linden, T. Reinhard, L. Stenzel, A. Swoboda, M. Grundner, and S. Mardazad, The SyTen toolkit, http://syten.eu.

[84] C. Hubig, I. P. McCulloch, U. Schollwöck, and F. A. Wolf, Strictly single-site DMRG algorithm with subspace expansion, Phys. Rev. B **91**, 155115 (2015).